

A Manifold Perspective on the Statistical Generalization of Graph Neural Networks

Zhiyang Wang *

Dept. of Electrical and Systems Eng.
University of Pennsylvania
Philadelphia, PA 19104
zhiyangw@seas.upenn.edu

Juan Cerviño*

Dept. of Electrical and Systems Eng.
University of Pennsylvania
Philadelphia, PA 19104
jcervino@seas.upenn.edu

Alejandro Ribeiro

Dept. of Electrical and Systems Eng.
University of Pennsylvania
Philadelphia, PA 19104
aribeiro@seas.upenn.edu

Abstract

Convolutional neural networks have been successfully extended to operate on graphs, giving rise to Graph Neural Networks (GNNs). GNNs combine information from adjacent nodes by successive applications of graph convolutions. GNNs have been implemented successfully in various learning tasks while the theoretical understanding of their generalization capability is still in progress. In this paper, we leverage manifold theory to analyze the statistical generalization gap of GNNs operating on graphs constructed on sampled points from manifolds. We study the generalization gaps of GNNs on both node-level and graph-level tasks. We show that the generalization gaps decrease with the number of nodes in the training graphs, which guarantees the generalization of GNNs to unseen points over manifolds. We validate our theoretical results in multiple real-world datasets.

1 Introduction

Graph convolutional neural networks (GNNs) [1–3] have emerged as one of the leading tools for processing graph-structured data. There is abundant evidence of their empirical success across various fields, including but not limited to weather prediction [4], protein structure prediction in biochemistry [5, 6], resource allocation in wireless communications [7], social network analysis in sociology [8], point cloud in 3D model reconstruction [9] and learning simulators [10].

The effectiveness of GNNs relies on their empirical ability to *predict* over unseen data. This capability is evaluated theoretically with *statistical generalization* in deep learning theory [11], which quantifies the difference between the *empirical risk* (i.e. training error) and the *statistical risk* (i.e. testing error). Despite the abundant evidence of GNNs’ generalization capabilities in practice, developing concrete theories to explain their generalization is an active area of research. Many recent works have studied the generalization bounds of GNNs without any dependence on the underlying model responsible for generating the graph data [12–14]. Generalization analysis on graph classification, when graphs are drawn from random limit models, is also studied in a series of works [15–18]. In this work, we follow a similar methodology to formulate graph data on continuous topological spaces

*The authors contribute equally.

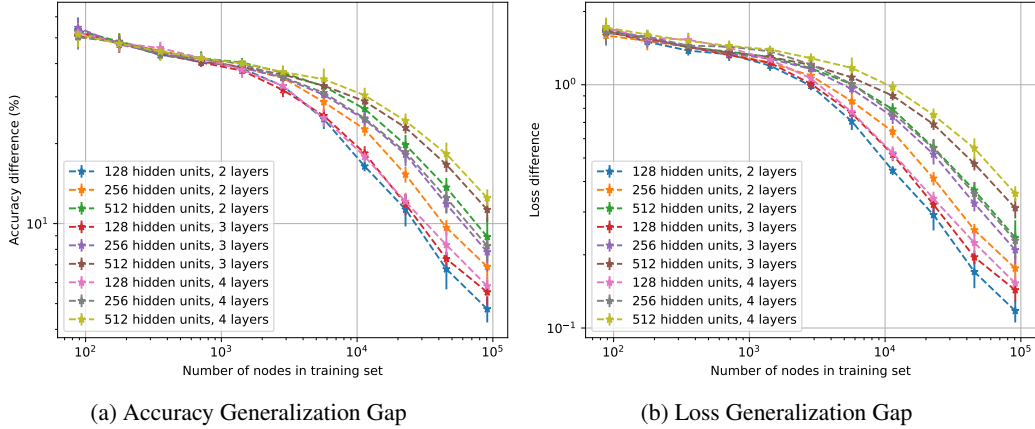


Figure 1: OBGN-Arxiv accuracy and loss generalization gaps. The GNN is trained over graphs with the number of nodes indicated on the x-axis, and the generalization gap (difference between the training and loss datasets) is measured, both in terms of the accuracy (Figure 1a), and the loss (Figure 1b) with which we trained – the cross-entropy loss. As can be seen, in both cases the generalization gap presents a logarithmically linear behavior with respect to the number of nodes.

– specifically, manifolds – which are realistic models that enable rigorous theoretical analysis and a deeper understanding of the behaviors of GNNs.

Specifically, we explore the generalization gap of GNNs through the lens of manifold theory on both node level and graph level tasks. The graphs are constructed based on points randomly sampled from underlying manifolds, indicating that the manifold can be viewed as a statistical model for these discretely sampled points. As convolutional neural network architectures have been established over manifolds [19], the convergence of GNNs to manifold neural networks (MNNs) facilitates a detailed generalization analysis over GNNs. We demonstrate that, with an appropriate graph construction (Definition 2 or Definition 3), the generalization gap between empirical and statistical risks decreases with the number of sampled points in the graphs while increasing with the manifold dimension. The main findings of this paper (Theorem 1 and Theorem 2) provide a unified approach, showing that GNNs can effectively generalize to other unseen data over the manifold.

Theorem (Informal, Node classification on Gaussian kernel based graphs). *Consider a graph constructed with N randomly sampled points over a d -dimensional manifold \mathcal{M} with respect to the measure μ over the manifold. Then, with probability $1 - \delta$ the generalization gap (GA) of a GNN with L layers and F features in each layer trained to predict the node labels on this graph satisfies*

$$GA \approx \mathcal{O} \left(\frac{LF^{L-1}}{\sqrt{N}} \left(\frac{\log 1/\delta}{N} \right)^{\frac{1}{d+4}} + F^L \left(\frac{\log N}{N} \right)^{\frac{1}{d}} \right). \quad (1)$$

Simulations on the ArXiv dataset [20] further validate our theoretical results as Figure 1 shows. Both the accuracy and loss generalization gaps decrease approximately linearly with the number of nodes in the logarithmic scale. We provide generalization bounds on both node and graph levels. For node level tasks, the generalization guarantees that a GNN trained on finitely sampled points over the manifold can accurately predict the labels of other unseen points over the manifold. For graph level tasks, the generalization assures that a GNN trained to classify graphs sampled from different manifolds can predict the labels of other unseen graphs sampled from these manifolds.

2 Related works

2.1 Generalization bounds of GNNs

Node level tasks We first give a brief recap of the generalization bounds of GNNs on node level tasks. In [12], the authors give a generalization bound of GNNs with a Vapnik–Chervonenkis

dimension of GNNs. The authors in [14] analyze the generalization of a single-layer GNN based on stability analysis, which is further extended to a multi-layer GNN in [21]. In [22], the authors give a novel PAC-Bayesian analysis on the generalization bound of GNNs across arbitrary subgroups of training and testing datasets. The authors derive generalization bounds for GNNs via transductive uniform stability and transductive Rademacher complexity in [23–25]. The authors in [26] propose a size generalization analysis of GNNs correlated to the discrepancy between local distributions of graphs. Different from these works, we consider a continuous manifold model when generating the graph data, which is theoretically powerful and realistic when characterizing real-world data.

Graph level tasks There are also related works on the generalization analysis of GNNs on graph level tasks. In [13], the authors form the generalization bound via Rademacher complexity. The authors in [27] build a PAC-Bayes framework to analyze the generalization capabilities of graph convolutional networks [28] and message-passing GNNs [29], based on which the authors in [30] improve the results and prove a lower bound. The works in [16–18] are most related to ours, which also consider the generalization of GNNs on a graph limit model. Different from our setting, the authors see the graph limit as a random continuous model. They study the generalization of graph classification problems with message-passing GNNs with graphs belonging to the same category sampled from a continuous limit model. The generalization bound grows with the model complexity and decreases with the number of nodes in the graph. We show that a GNN trained on a single graph sampled from each manifold is enough, and can generalize and classify unseen graphs sampled from the manifold set.

2.2 Neural networks on manifolds

Geometric deep learning has been proposed in [31] with neural network architectures raised in manifold space. The authors in [32] and [33] provide neural network architectures for manifold-valued data. In [34] and [19], the authors define convolutional operation over manifolds and see the manifold convolution as a generalization of graph convolution, which establishes the limit of neural networks on large-scale graphs as manifold neural networks (MNNs). The authors in [35] further establish the relationship between GNNs and MNNs with non-asymptotic convergence results for different graph constructions.

3 Preliminaries

3.1 Graph neural networks

Setup An undirected graph $\mathbf{G} = (\mathcal{V}, \mathcal{E}, \mathcal{W})$ contains a node set \mathcal{V} with N nodes and an edge set $\mathcal{E} \subseteq \mathcal{V} \times \mathcal{V}$. The weight function $\mathcal{W} : \mathcal{E} \rightarrow \mathbb{R}$ assigns weight values to the edges. We define the Graph Laplacian $\mathbf{L} = \text{diag}(\mathbf{A}\mathbf{1}) - \mathbf{A}$ where $\mathbf{A} \in \mathbb{R}^{N \times N}$ is the adjacency matrix. Graph signals are defined as functions mapping nodes to a feature value $\mathbf{x} \in \mathbb{R}^N$.

Graph convolutions and frequency response A graph convolutional filter $\mathbf{h}_{\mathbf{G}}$ is composed of consecutive graph shifts by graph Laplacian, defined as $\mathbf{h}_{\mathbf{G}}(\mathbf{L})\mathbf{x} = \sum_{k=0}^{K-1} h_k \mathbf{L}^k \mathbf{x}$ with $\{h_k\}_{k=0}^{K-1}$ as filter parameters. We replace \mathbf{L} with eigendecomposition $\mathbf{L} = \mathbf{V}\mathbf{\Lambda}\mathbf{V}^H$, where \mathbf{V} is the eigenvector matrix and $\mathbf{\Lambda}$ is a diagonal matrix with eigenvalues $\{\lambda_{i,N}\}_{i=1}^N$ as the entries. The spectral representation of a graph filter is

$$\mathbf{V}^H \mathbf{h}_{\mathbf{G}}(\mathbf{L})\mathbf{x} = \sum_{k=0}^{K-1} h_k \mathbf{\Lambda}^k \mathbf{V}^H \mathbf{x} = \hat{h}(\mathbf{\Lambda}) \mathbf{V}^H \mathbf{x}. \quad (2)$$

This leads to a point-wise frequency response of the graph convolution as $\hat{h}(\lambda) = \sum_{k=0}^{K-1} h_k \lambda^k$.

Graph neural networks A graph neural network (GNN) is a layered architecture, where each layer consists of a bank of graph convolutional filters followed by a point-wise nonlinearity $\sigma : \mathbb{R} \rightarrow \mathbb{R}$. Specifically, the l -th layer of a GNN that produces F_l output features $\{\mathbf{x}_l^p\}_{p=1}^{F_l}$ with F_{l-1} input

features $\{\mathbf{x}_{l-1}^q\}_{q=1}^{F_{l-1}}$ is written as

$$\mathbf{x}_l^p = \sigma \left(\sum_{q=1}^{F_{l-1}} \mathbf{h}_{\mathbf{G}}^{lpq}(\mathbf{L}) \mathbf{x}_{l-1}^q \right), \quad (3)$$

for each layer $l = 1, 2, \dots, L$. The graph filter $\mathbf{h}_{\mathbf{G}}^{lpq}(\mathbf{L})$ maps the q -th feature of layer $l-1$ to the p -th feature of layer l . We denote the GNN as a mapping $\Phi_{\mathbf{G}}(\mathbf{H}, \mathbf{L}, \mathbf{x})$, where $\mathbf{H} \in \mathcal{H} \subset \mathbb{R}^P$ denotes a set of the graph filter coefficients at all layers and \mathcal{H} denotes the set of all possible parameter sets.

3.2 Manifold neural networks

Setup We consider a d -dimensional compact, smooth and differentiable submanifold \mathcal{M} embedded in \mathbb{R}^M . This induces a probability measure μ over the manifold with density function $\rho : \mathcal{M} \rightarrow (0, \infty)$, assumed to be bounded as $0 < \rho_{\min} \leq \rho(x) \leq \rho_{\max} < \infty$ for all $x \in \mathcal{M}$. The manifold data supported on each point $x \in \mathcal{M}$ is defined by scalar functions $f : \mathcal{M} \rightarrow \mathbb{R}$ [34]. We use $L^2(\mathcal{M})$ to denote L^2 functions over \mathcal{M} with respect to measure μ . The manifold with probability density function ρ is equipped with a weighted Laplace operator [36], generalizing the Laplace-Beltrami operator as

$$\mathcal{L}_{\rho} f = -\frac{1}{2\rho} \operatorname{div}(\rho^2 \nabla f), \quad (4)$$

with div denoting the divergence operator of \mathcal{M} and ∇ denoting the gradient operator of \mathcal{M} [31, 37].

Manifold convolutions and frequency responses The manifold convolution operation is defined relying on the Laplace operator \mathcal{L}_{ρ} and on the heat diffusion process over the manifold [34]. For a function $f \in L^2(\mathcal{M})$, the manifold diffusion can be explicitly written as $e^{-\mathcal{L}_{\rho}} f$. A manifold convolutional filter [34] can be defined in a diffuse-and-sum manner as

$$g(x) = \mathbf{h}(\mathcal{L}_{\rho}) f(x) = \sum_{k=0}^{K-1} h_k e^{-k\mathcal{L}_{\rho}} f(x), \quad (5)$$

with the k -th diffusion scaled with a filter parameter $h_k \in \mathbb{R}$. We consider the case in which the Laplace operator is self-adjoint and positive-semidefinite and the manifold \mathcal{M} is compact, in this case, \mathcal{L}_{ρ} has real, positive and discrete eigenvalues $\{\lambda_i\}_{i=1}^{\infty}$, written as $\mathcal{L}_{\rho} \phi_i = \lambda_i \phi_i$ where ϕ_i is the eigenfunction associated with eigenvalue λ_i . The eigenvalues are ordered in increasing order as $0 < \lambda_1 \leq \lambda_2 \leq \lambda_3 \leq \dots$, and the eigenfunctions are orthonormal and form an eigenbasis of $L^2(\mathcal{M})$. When mapping a manifold signal onto the eigenbasis $[\hat{f}]_i = \langle f, \phi_i \rangle_{\mathcal{M}}$, the manifold convolution can be written in the spectral domain as

$$[\hat{g}]_i = \sum_{k=0}^{K-1} h_k e^{-k\lambda_i} [\hat{f}]_i. \quad (6)$$

Hence, the frequency response of manifold filter is given by $\hat{h}(\lambda) = \sum_{k=0}^{K-1} h_k e^{-k\lambda}$.

Manifold neural networks A manifold neural network (MNN) is constructed by cascading L layers, each of which contains a bank of manifold convolutional filters and a pointwise nonlinearity $\sigma : \mathbb{R} \rightarrow \mathbb{R}$. The output manifold function of each layer $l = 1, 2, \dots, L$ can be explicitly denoted as

$$f_l^p(x) = \sigma \left(\sum_{q=1}^{F_{l-1}} \mathbf{h}_l^{pq}(\mathcal{L}_{\rho}) f_{l-1}^q(x) \right), \quad (7)$$

where f_{l-1}^q , $1 \leq q \leq F_{l-1}$ is the q -th input feature from layer $l-1$ and f_l^p , $1 \leq p \leq F_l$ is the p -th output feature of layer l . We denote MNN as a mapping $\Phi(\mathbf{H}, \mathcal{L}_{\rho}, f)$, where $\mathbf{H} \in \mathcal{H} \subset \mathbb{R}^P$ is a collective set of filter parameters in all the manifold convolutional filters.

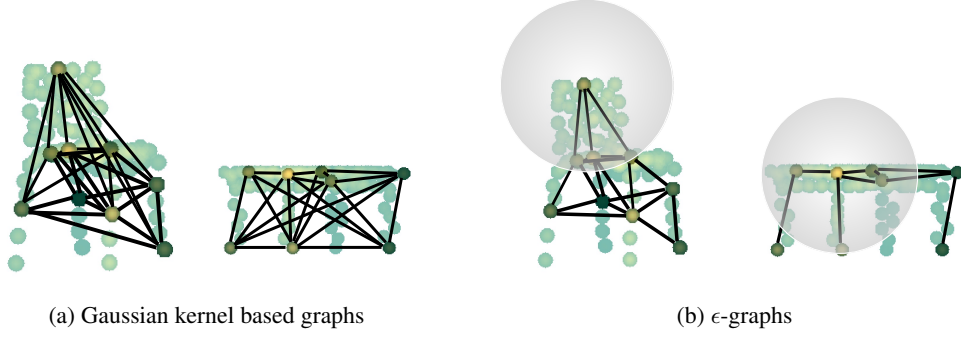


Figure 2: Illustration of the constructed graphs on points sampled over a chair and a table model.

4 Generalization analysis of GNNs based on manifold

We consider a manifold \mathcal{M} as defined in Section 3.2, equipped with a weighted Laplace operator \mathcal{L}_ρ as (4). Since functions $f \in L^2(\mathcal{M})$ are used to characterize information over manifold \mathcal{M} , we restrict our analysis to a finite-dimensional subset of $L^2(\mathcal{M})$ up to some eigenvalue of \mathcal{L}_ρ , which is defined as a bandlimited signal.

Definition 1. A manifold signal $f \in L^2(\mathcal{M})$ is bandlimited if there exists some $\lambda > 0$ such that for all eigenpairs $\{\lambda_i, \phi_i\}_{i=1}^\infty$ of the weighted Laplacian \mathcal{L}_ρ when $\lambda_i > \lambda$, we have $\langle f, \phi_i \rangle_{\mathcal{M}} = 0$.

Suppose we are given a set of N i.i.d. randomly sampled points $X_N = \{x_i\}_{i=1}^N$ over \mathcal{M} , with $x_i \in \mathcal{M}$ sampled according to measure μ . We construct a graph $\mathbf{G}(\mathcal{V}, \mathcal{E}, \mathcal{W})$ on these N sampled points X_N , where each point x_i is a vertex of graph \mathbf{G} , i.e. $\mathcal{V} = X_N$. Each pair of vertices (x_i, x_j) is connected with an edge while the weight attached to the edge $\mathcal{W}(x_i, x_j)$ is determined by a kernel function K_ϵ . The kernel function is decided by the Euclidean distance $\|x_i - x_j\|$ between these two points. The graph Laplacian denoted as \mathbf{L}_N can be calculated based on the weight function [38]. The constructed graph Laplacian with an appropriate kernel function has been proved to approximate the Laplace operator \mathcal{L}_ρ of \mathcal{M} [39–41]. We present the following two definitions of K_ϵ .

Definition 2 (Gaussian kernel based graph [40]). The graph $\mathbf{G}(X_N, \mathcal{E}, \mathcal{W})$ can be constructed as a dense graph degree when the kernel function is defined as

$$\mathcal{W}(x_i, x_j) = K_\epsilon \left(\frac{\|x_i - x_j\|^2}{\epsilon} \right) = \frac{1}{N} \frac{1}{\epsilon^{d/2+1} (4\pi)^{d/2}} e^{-\frac{\|x_i - x_j\|^2}{4\epsilon}}, \quad (x_i, x_j) \in \mathcal{E}. \quad (8)$$

The weight function of a Gaussian kernel based graph is defined on unbounded support (i.e. $[0, \infty)$), which connects x_i and x_j regardless of the distance between them. This results in a dense graph with N^2 edges. In particular, this Gaussian kernel based graph has been widely used to define the weight value function due to the good approximation properties of the corresponding graph Laplacians to the manifold Laplace operator [40–42].

Definition 3 (ϵ -graph [39]). The graph $\mathbf{G}(X_N, \mathcal{E}, \mathcal{W})$ can be constructed as an ϵ -graph with the kernel function defined as

$$\mathcal{W}(x_i, x_j) = K_\epsilon \left(\frac{\|x_i - x_j\|^2}{\epsilon} \right) = \frac{1}{N} \frac{d+2}{\epsilon^{d/2+1} \alpha_d} \mathbb{1}_{[0,1]} \left(\frac{\|x_i - x_j\|^2}{\epsilon} \right), \quad (x_i, x_j) \in \mathcal{E}, \quad (9)$$

where α_d is the volume of a unit ball of dimension d and $\mathbb{1}$ is the characteristic function.

The weight function of an ϵ -graph is defined on a bounded support, i.e., only nodes that are within a certain distance of one another can be connected by an edge. It has also been shown to provide a good approximation of the manifold Laplace operator [39]. Figure 2 gives an illustration of both Gaussian kernel based graphs and ϵ -graphs sampled from point cloud models [43].

4.1 Manifold label prediction via node label prediction

Suppose we have an input manifold signal $f \in L^2(\mathcal{M})$ and a label (i.e. target) manifold signal $g \in L^2(\mathcal{M})$ over \mathcal{M} . With an MNN $\Phi(\mathbf{H}, \mathcal{L}_\rho, \cdot)$, we predict the target value $g(x)$ based on input

$f(x)$ at each point $x \in \mathcal{M}$. By sampling N points X_N over this manifold, we can approximate this problem in a discrete graph domain. Consider a graph $\mathbf{G}(X_N, \mathcal{E}, \mathcal{W})$ constructed with X_N as either a Gaussian kernel based graph (Definition 2) or an ϵ -graph (Definition 3) equipped with the graph Laplacian \mathbf{L}_N . Suppose we are given graph signal $\{\mathbf{x}, \mathbf{y}\}$ sampled from $\{f, g\}$ to train a GNN $\Phi_{\mathbf{G}}(\mathbf{H}, \mathbf{L}_N, \cdot)$, explicitly written as

$$[\mathbf{x}]_i = f(x_i), \quad [\mathbf{y}]_i = g(x_i) \quad \text{for all } x_i \in X_N. \quad (10)$$

We assume that the filters in MNN $\Phi(\mathbf{H}, \mathcal{L}_\rho, \cdot)$ and GNN $\Phi_{\mathbf{G}}(\mathbf{H}, \mathbf{L}_N, \cdot)$ are low-pass filters, which are defined explicitly as follows.

Definition 4. A filter is a low-pass filter if its frequency response satisfies

$$|\hat{h}(\lambda)| = \mathcal{O}(\lambda^{-d}), \quad \lambda \in (0, \infty). \quad (11)$$

To introduce the first of our two main results, we require the introduction of two assumptions.

AS 1. (Normalized Lipschitz nonlinearity) The nonlinearity σ is normalized Lipschitz continuous, i.e., $|\sigma(a) - \sigma(b)| \leq |a - b|$, with $\sigma(0) = 0$.

AS 2. (Normalized Lipschitz loss function) The loss function ℓ is normalized Lipschitz continuous, i.e., $|\ell(y_i, y) - \ell(y_j, y)| \leq |y_i - y_j|$, with $\ell(y, y) = 0$.

Assumption 1 is satisfied by most activations used in practice such as ReLU, modulus and sigmoid.

The generalization gap is evaluated between the *empirical risk* over the discrete graph model and the *statistical risk* over manifold model, with the manifold model viewed as a statistical model since the expectation of the sampled point is with respect to the measure μ over the manifold. The empirical risk over the sampled graph that we trained to minimize is therefore defined as

$$R_{\mathbf{G}}(\mathbf{H}) = \frac{1}{N} \sum_{i=1}^N \ell([\Phi_{\mathbf{G}}(\mathbf{H}, \mathbf{L}_N, \mathbf{x})]_i, [\mathbf{y}]_i). \quad (12)$$

The statistical risk over the manifold is defined as

$$R_{\mathcal{M}}(\mathbf{H}) = \int_{\mathcal{M}} \ell(\Phi(\mathbf{H}, \mathcal{L}_\rho, f)(x), g(x)) d\mu(x). \quad (13)$$

The generalization gap is defined to be

$$GA = \min_{\mathbf{H} \in \mathcal{H}} R_{\mathcal{M}}(\mathbf{H}) - \min_{\mathbf{H} \in \mathcal{H}} R_{\mathbf{G}}(\mathbf{H}). \quad (14)$$

Theorem 1. Suppose the GNN and MNN with low-pass filters (Definition 4) have L layers with F features in each layer and the input signal is bandlimited (Definition 1). Under Assumptions 1 and 2 it holds in probability at least $1 - \delta$ that

$$GA \leq LF^{L-1} \left(C_1 \frac{\epsilon}{\sqrt{N}} + C_2 \frac{\sqrt{\log(1/\delta)}}{N} \right) + F^L C_3 \left(\frac{\log N}{N} \right)^{\frac{1}{d}} \quad (15)$$

1. When the graph is constructed with a Gaussian kernel (8), then $\epsilon \sim \left(\frac{\log(C/\delta)}{N} \right)^{\frac{1}{d+4}}$.
2. When the graph is constructed as an ϵ -graph as (9), then $\epsilon \sim \left(\frac{\log(CN/\delta)}{N} \right)^{\frac{1}{d+4}}$.

Proof. See Appendix D for proof and the definitions of C_1 , C_2 and C_3 . \square

Theorem 1 shows that the generalization gap decreases approximately linearly with the number of nodes N in the logarithmic scale. It also increases with the dimension of the underlying manifold d . Another observation is that the generalization gap scales with the size of GNN architectures. Specifically, it scales polynomially with the number of features F , while the exponent depends on the number of layers L . This generalization result attests that when the graph is supported on a manifold, a GNN trained on this discrete graph model can approximate the MNN performance. GNNs trained on these finite sampled points can generalize to predict the labels of other unseen points over the manifold with large enough nodes in the graph. To generalize effectively over a manifold with a higher dimension, more sampled points are required to construct the graph to guarantee the generalization capability.

4.2 Manifold classification via graph classification

Suppose we have a set of manifolds $\{\mathcal{M}_k\}_{k=1}^K$, each of which is d_k -dimensional, smooth, compact, differentiable and embedded in \mathbb{R}^M with measure μ_k . Each manifold \mathcal{M}_k equipped with a weighted Laplace operator $\mathcal{L}_{\rho,k}$ is labeled with $y_k \in \mathbb{R}$. We assume to have access to N_k randomly sampled points according to measure μ_k over each manifold \mathcal{M}_k and construct K graphs $\{\mathbf{G}_k\}_{k=1}^K$ with graph Laplacian $\mathbf{L}_{N,k}$. The GNN $\Phi_{\mathbf{G}}(\mathbf{H}, \mathbf{L}_{N,\cdot}, \mathbf{x}_\cdot)$ is trained on this set of graphs with \mathbf{x}_k as the input graph signal sampled from the manifold signal $f_k \in L^2(\mathcal{M}_k)$ and $y_k \in \mathbb{R}$ as the scalar target label. The final output of the GNN is set to be the average of the output signal values on each node while the output of MNN $\Phi(\mathbf{H}, \mathcal{L}_{\rho,\cdot}, f_\cdot)$ is the statistical average value of the output signal over the manifold. A loss function ℓ evaluates the difference between the output of GNN and MNN with the target label. The empirical risk of the GNN is

$$R_{\mathbf{G}}(\mathbf{H}) = \sum_{k=1}^K \ell \left(\frac{1}{N_k} \sum_{i=1}^{N_k} [\Phi(\mathbf{H}, \mathbf{L}_{N,k}, \mathbf{x}_k)]_i, y_k \right). \quad (16)$$

While the output of MNN is the average value over the manifold, the statistical risk is defined based on the loss evaluated between the MNN output and the label as

$$R_{\mathcal{M}}(\mathbf{H}) = \sum_{k=1}^K \ell \left(\int_{\mathcal{M}_k} \Phi(\mathbf{H}, \mathcal{L}_{\rho,k}, f_k)(x) d\mu_k(x), y_k \right). \quad (17)$$

The generalization gap is therefore

$$GA = \min_{\mathbf{H} \in \mathcal{H}} R_{\mathcal{M}}(\mathbf{H}) - \min_{\mathbf{H} \in \mathcal{H}} R_{\mathbf{G}}(\mathbf{H}). \quad (18)$$

Theorem 2. Suppose the GNN and MNN with low-pass filters (Definition 4) have L layers with F features in each layer and the input signal is bandlimited (Definition 1). Under Assumptions 1 and 2 it holds in probability at least $1 - \delta$ that

$$GA \leq LF^{L-1} \sum_{k=1}^K \left(\frac{C_1}{\sqrt{N_k}} \epsilon + C_2 \frac{\sqrt{\log(1/\delta)}}{N_k} \right) + F^L C_3 \sum_{k=1}^K \left(\frac{\log N_k}{N_k} \right)^{\frac{1}{d_k}} \quad (19)$$

1. When the graph is constructed with a Gaussian kernel (8), then $\epsilon \sim \left(\frac{\log(C/\delta)}{N_k} \right)^{\frac{1}{d_k+4}}$.
2. When the graph is constructed as an ϵ -graph as (9), then $\epsilon \sim \left(\frac{\log(CN_k/\delta)}{N_k} \right)^{\frac{1}{d_k+4}}$.

Proof. See Appendix E for proof and the definitions of C_1 , C_2 and C_3 . \square

Theorem 2 shows that a single graph sampled from the underlying manifold with large enough sampled points N can provide an effective approximation to classify the manifold itself. The generalization gap also attests that the trained GNN can generalize to classify other unseen graphs sampled from the same manifold. Similar to the generalization result in node-level tasks, the generalization gap decreases with the number of points sampled over each manifold while increasing with the manifold dimension. A higher dimensional manifold, i.e. higher complexity, needs more samples to guarantee the generalization. The generalization gap also scales with the size of GNN architecture polynomially with the number of features and exponentially with the number of layers.

5 Experiments

Node classification In this section, we empirically study the generalization gap in 8 real-world datasets. The task is to predict the label of a node given a set of features. The datasets vary in the number of nodes from 169, 343 to 3, 327, and in the number of edges from 1, 166, 243 to 9, 104. The feature dimension also varies from 8, 415 to 300 features, and the number of classes of the node label from 40 to 3. We consider the following datasets: *OGBN-Arxiv* [20, 44], *Cora* [45], *CiteSeer* [45],

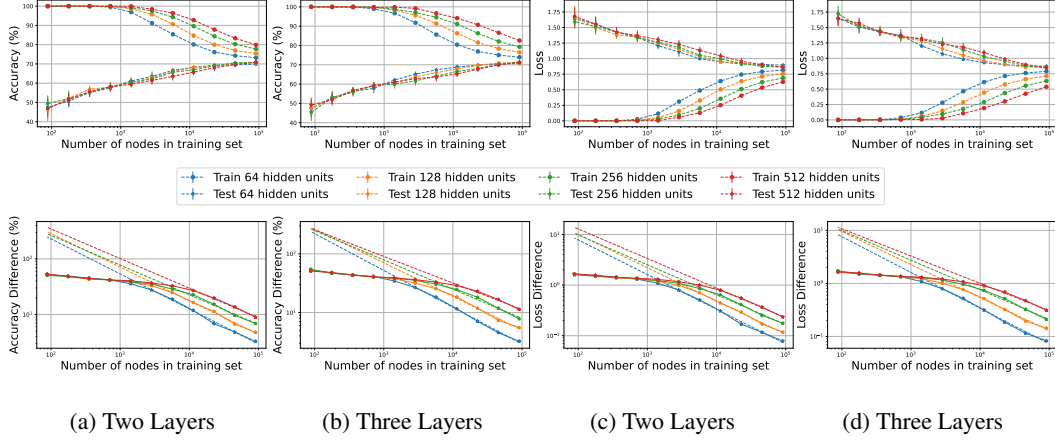


Figure 3: In the top row, we plot the difference in the accuracy and loss for columns 3a, 3b and 3c, 3d, respectively. On the bottom row, we plot the actual train and test values of the accuracy (3a, 3b), and the loss (3c, 3d). The plots are for the Arxiv dataset and $\{64, 128, 256, 512\}$ hidden units. For the bottom row, we also calculate the linear fit for the values whose training accuracy is below 95%, showing that our linear bound on the logarithm of the generalization gap for the logarithm of the number of nodes shares the same rate shown in Theorem 1.

PubMed [45], *Coauthors CS* [46], *Coauthors Physics* [46], *Amazon-rating* [47], and *Roman-Empire* [47], details of the datasets can be found in Table 2. In all cases, we vary the number of nodes in the training set by partitioning it in $\{1, 2, 4, 8, 16, 32, 64, 128, 256, 512, 1024\}$ partitions when possible. For both the training and testing sets, we computed the loss in *cross-entropy loss*, and the accuracy in percentage (%).

Our main goal is to show that the rate presented in Theorem 1 holds in practice. That is to say, if we plot the logarithm of the generalization gap as a function of the logarithm of the number of nodes we see a linear rate. To be consistent with the theory, we also want to show that if the number of layers or the size of the features increases, so does the generalization gap.

In Figure 3, we plot the generalization gap of the accuracy in the logarithmic scale for a two-layered GNN (Figure 3a), and for a three-layered GNN (Figure 3b). On the upper side, we can see that the generalization bound decreases with the number of nodes and that outside of the strictly overfitting regime (when the training loss is below 95%), the generalization gap shows a linear decay, as depicted in the dashed line. The same behavior can be seen in plots 3c, and 3d which correspond to the loss for 2 and 3 layered GNNs. As predicted by our theory, the generalization gap increases with the

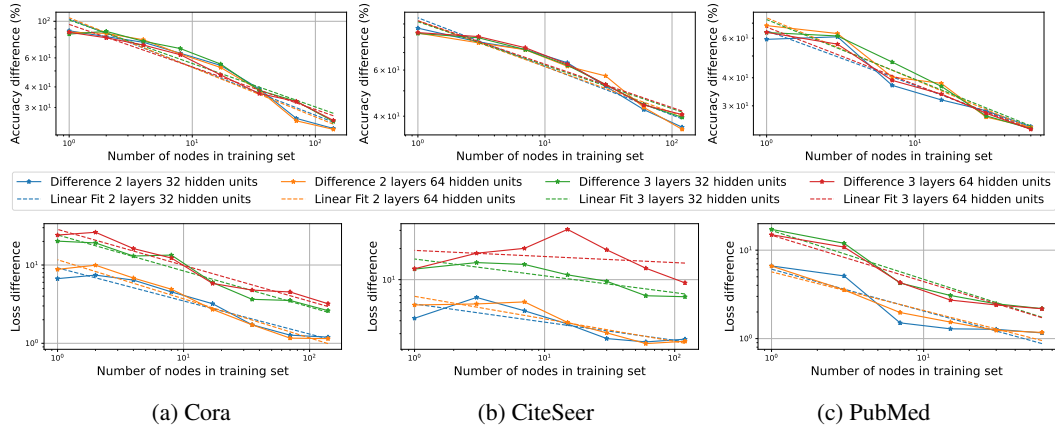


Figure 4: Generalization gap as a function of the number of nodes in the training set for accuracy (top) and loss (bottom) for the Cora, CiteSeer, and PubMed datasets.

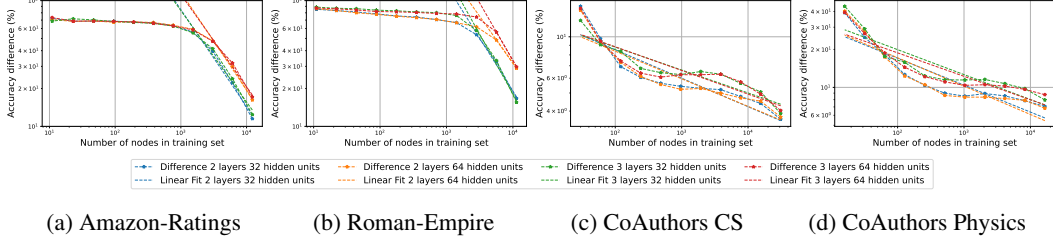


Figure 5: Accuracy generalization gap as a function of the number of nodes in the training set for the Amazon-Ratings, Roman-Empire, CoAuthors CS, and CoAuthors Physics datasets.

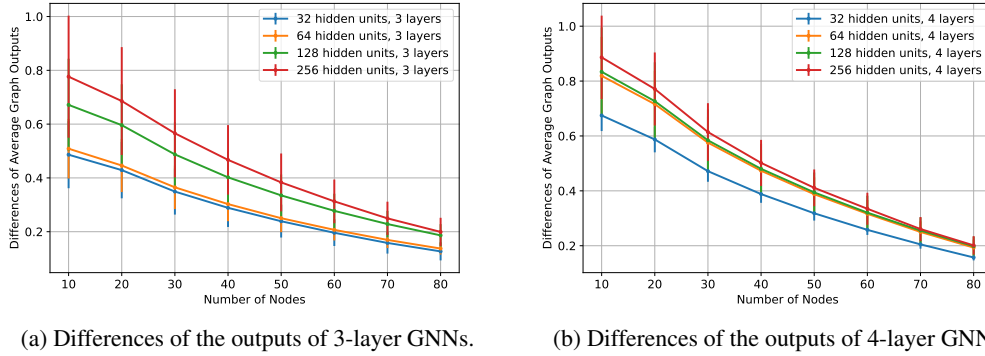


Figure 6: Generalization gap as a function of number of nodes for average GNN output differences for graph classification over ModelNet10.

number of features and layers in the GNN (see also Figure 1). The behavior of the training and testing accuracy as a function of the number of nodes is intuitive. For the training loss, when the number of nodes in the training set is small, the GNN can overfit the training data. As the number of features increases, the GNN’s capacity to overfit also increases.

In Figures 4, and 5 we present the accuracy generalization gaps for 2 and 3 layers with 32 and 64 features. In the overfitting regime, the rate of our generalization bound seems to hold – decreases linearly with the number of nodes in the logarithmic scale. In the non-overfitting regime, our rate holds for the points whose training accuracy is below 95%. Also, we validate that the bound increases both with the number of features, as well as the number of layers.

In Table 1 we present the Pearson correlation coefficient to measure the linear relationships in the generalization gaps of a 2 layers GNN with 64 hidden units in all datasets considered. In almost every case, the coefficient is above 0.95 which translates into a strong linear correlation. In Appendix F we explain how we computed these values. As seen in the experiment, the GNN generalization gap experiences a linear decay with respect to the number of nodes in the logarithmic scale. The bound presented in Theorem 1 is an upper bound on the generalization gap, whose rate can be seen to match the one seen in practice both for the loss, as well as the accuracy gaps.

Dataset	Pearson Correlation Coefficient
OGBN-Arxiv	−0.9980
Cora	−0.9686
CiteSeer	−0.9534
PubMed	−0.9761
CS	−0.8969
Physics	−0.9145
Amazon	−0.9972
Roman	−1.0000

Table 1: Pearson correlation for 2 layer, 64 hidden units GNNs measured on the accuracy generalization gap.

Graph classification We evaluate the generalization gap on graph prediction using the ModelNet10 dataset [43]. We set the coordinates of each point as input graph signals, and the weights of the edges are calculated based on the Euclidean distance between the nodes. The generalization gap is calculated by training GNNs on graphs with $N = 10, 20, \dots, 80$ sampled points, and plotting the

differences between the average output of the trained GNNs on the trained graph and a testing graph with size $N = 100$. Figure 6a shows the generalization gaps for GNNs with 3 layers and Figure 6b shows the results of GNNs with 4 layers. We can see that the output differences between the GNNs decrease with the number of nodes and scale with the size of the GNN architectures. This verifies the claims of Theorem 2. In Appendix F, we present experiment results on more model datasets.

6 Conclusion

We study the statistical generalization of GNNs from a manifold perspective. We considered graphs sampled from manifolds and proved that GNNs can effectively generalize to unseen data from the manifolds when the number of sampled points is large enough. We validate our results both on node-level and graph-level classification tasks with real-world datasets. The impact of this paper is to show a better understanding of GNN generalization capabilities from a statistical perspective relying on a continuous model. Our work also motivates the practical design of large-scale GNNs. For future work, we will study the switching behavior between the over-fitting, and non-over-fitting regimes of node classification.

References

- [1] Franco Scarselli, Marco Gori, Ah Chung Tsoi, Markus Hagenbuchner, and Gabriele Monfardini. The graph neural network model. *IEEE transactions on neural networks*, 20(1):61–80, 2008.
- [2] Michaël Defferrard, Xavier Bresson, and Pierre Vandergheynst. Convolutional neural networks on graphs with fast localized spectral filtering. *Advances in neural information processing systems*, 29, 2016.
- [3] Joan Bruna, Wojciech Zaremba, Arthur Szlam, and Yann LeCun. Spectral networks and locally connected networks on graphs. *arXiv preprint arXiv:1312.6203*, 2013.
- [4] Remi Lam, Alvaro Sanchez-Gonzalez, Matthew Willson, Peter Wirsberger, Meire Fortunato, Ferran Alet, Suman Ravuri, Timo Ewalds, Zach Eaton-Rosen, Weihua Hu, et al. Learning skillful medium-range global weather forecasting. *Science*, 382(6677):1416–1421, 2023.
- [5] John Jumper, Richard Evans, Alexander Pritzel, Tim Green, Michael Figurnov, Olaf Ronneberger, Kathryn Tunyasuvunakool, Russ Bates, Augustin Žídek, Anna Potapenko, et al. Highly accurate protein structure prediction with alphafold. *Nature*, 596(7873):583–589, 2021.
- [6] Alexey Strokach, David Becerra, Carles Corbi-Verge, Albert Perez-Riba, and Philip M Kim. Fast and flexible protein design using deep graph neural networks. *Cell systems*, 11(4):402–411, 2020.
- [7] Zhiyang Wang, Mark Eisen, and Alejandro Ribeiro. Learning decentralized wireless resource allocations with graph neural networks. *IEEE Transactions on Signal Processing*, 70:1850–1863, 2022.
- [8] Wenqi Fan, Yao Ma, Qing Li, Jianping Wang, Guoyong Cai, Jiliang Tang, and Dawei Yin. A graph neural network framework for social recommendations. *IEEE Transactions on Knowledge and Data Engineering*, 34(5):2033–2047, 2020.
- [9] Weijing Shi and Raj Rajkumar. Point-gnn: Graph neural network for 3d object detection in a point cloud. In *Proceedings of the IEEE/CVF conference on computer vision and pattern recognition*, pages 1711–1719, 2020.
- [10] Meire Fortunato, Tobias Pfaff, Peter Wirsberger, Alexander Pritzel, and Peter Battaglia. Multiscale meshgraphnets. In *ICML 2022 2nd AI for Science Workshop*, 2022.
- [11] Kenji Kawaguchi, Leslie Pack Kaelbling, and Yoshua Bengio. Generalization in deep learning. *arXiv preprint arXiv:1710.05468*, 1(8), 2017.
- [12] Franco Scarselli, Ah Chung Tsoi, and Markus Hagenbuchner. The vapnik–chervonenkis dimension of graph and recursive neural networks. *Neural Networks*, 108:248–259, 2018.
- [13] Vikas Garg, Stefanie Jegelka, and Tommi Jaakkola. Generalization and representational limits of graph neural networks. In *International Conference on Machine Learning*, pages 3419–3430. PMLR, 2020.
- [14] Saurabh Verma and Zhi-Li Zhang. Stability and generalization of graph convolutional neural networks. In *Proceedings of the 25th ACM SIGKDD International Conference on Knowledge Discovery & Data Mining*, pages 1539–1548, 2019.
- [15] Luana Ruiz, Luiz FO Chamon, and Alejandro Ribeiro. Transferability properties of graph neural networks. *IEEE Transactions on Signal Processing*, 2023.
- [16] Sohir Maskey, Ron Levie, Yunseok Lee, and Gitta Kutyniok. Generalization analysis of message passing neural networks on large random graphs. *Advances in neural information processing systems*, 35:4805–4817, 2022.
- [17] Sohir Maskey, Gitta Kutyniok, and Ron Levie. Generalization bounds for message passing networks on mixture of graphons. *arXiv preprint arXiv:2404.03473*, 2024.
- [18] Ron Levie. A graphon-signal analysis of graph neural networks. *Advances in Neural Information Processing Systems*, 36, 2024.

- [19] Zhiyang Wang, Luana Ruiz, and Alejandro Ribeiro. Convolutional neural networks on manifolds: From graphs and back. In *2022 56th Asilomar Conference on Signals, Systems, and Computers*, pages 356–360. IEEE, 2022.
- [20] Kuansan Wang, Zhihong Shen, Chiyuan Huang, Chieh-Han Wu, Yuxiao Dong, and Anshul Kanakia. Microsoft academic graph: When experts are not enough. *Quantitative Science Studies*, 1(1):396–413, 2020.
- [21] Xianchen Zhou and Hongxia Wang. The generalization error of graph convolutional networks may enlarge with more layers. *Neurocomputing*, 424:97–106, 2021.
- [22] Jiaqi Ma, Junwei Deng, and Qiaozhu Mei. Subgroup generalization and fairness of graph neural networks. *Advances in Neural Information Processing Systems*, 34:1048–1061, 2021.
- [23] Pascal Esser, Leena Chennuru Vankadara, and Debarghya Ghoshdastidar. Learning theory can (sometimes) explain generalisation in graph neural networks. *Advances in Neural Information Processing Systems*, 34:27043–27056, 2021.
- [24] Weilin Cong, Morteza Ramezani, and Mehrdad Mahdavi. On provable benefits of depth in training graph convolutional networks. *Advances in Neural Information Processing Systems*, 34:9936–9949, 2021.
- [25] Huayi Tang and Yong Liu. Towards understanding generalization of graph neural networks. In *International Conference on Machine Learning*, pages 33674–33719. PMLR, 2023.
- [26] Gilad Yehudai, Ethan Fetaya, Eli Meir, Gal Chechik, and Haggai Maron. From local structures to size generalization in graph neural networks. In *International Conference on Machine Learning*, pages 11975–11986. PMLR, 2021.
- [27] Renjie Liao, Raquel Urtasun, and Richard Zemel. A pac-bayesian approach to generalization bounds for graph neural networks. In *International Conference on Learning Representations*, 2020.
- [28] Thomas N Kipf and Max Welling. Semi-supervised classification with graph convolutional networks. In *International Conference on Learning Representations*, 2016.
- [29] Justin Gilmer, Samuel S Schoenholz, Patrick F Riley, Oriol Vinyals, and George E Dahl. Neural message passing for quantum chemistry. In *International conference on machine learning*, pages 1263–1272. PMLR, 2017.
- [30] Haotian Ju, Dongyue Li, Aneesh Sharma, and Hongyang R Zhang. Generalization in graph neural networks: Improved pac-bayesian bounds on graph diffusion. In *International Conference on Artificial Intelligence and Statistics*, pages 6314–6341. PMLR, 2023.
- [31] Michael M Bronstein, Joan Bruna, Yann LeCun, Arthur Szlam, and Pierre Vandergheynst. Geometric deep learning: going beyond euclidean data. *IEEE Signal Processing Magazine*, 34(4):18–42, 2017.
- [32] Federico Monti, Davide Boscaini, Jonathan Masci, Emanuele Rodola, Jan Svoboda, and Michael M Bronstein. Geometric deep learning on graphs and manifolds using mixture model cnns. In *Proceedings of the IEEE conference on computer vision and pattern recognition*, pages 5115–5124, 2017.
- [33] Rudrasis Chakraborty, Jose Bouza, Jonathan H Manton, and Baba C Vemuri. Manifoldnet: A deep neural network for manifold-valued data with applications. *IEEE Transactions on Pattern Analysis and Machine Intelligence*, 44(2):799–810, 2020.
- [34] Zhiyang Wang, Luana Ruiz, and Alejandro Ribeiro. Stability to deformations of manifold filters and manifold neural networks. *IEEE Transactions on Signal Processing*, pages 1–15, 2024.
- [35] Zhiyang Wang, Luana Ruiz, and Alejandro Ribeiro. Geometric graph filters and neural networks: Limit properties and discriminability trade-offs. *IEEE Transactions on Signal Processing*, 2024.
- [36] Alexander Grigor’yan. Heat kernels on weighted manifolds and applications. *Cont. Math*, 398(2006):93–191, 2006.

- [37] Gal Gross and Eckhard Meinrenken. *Manifolds, vector fields, and differential forms: an introduction to differential geometry*. Springer Nature, 2023.
- [38] Russell Merris. A survey of graph laplacians. *Linear and Multilinear Algebra*, 39(1-2):19–31, 1995.
- [39] Jeff Calder and Nicolas Garcia Trillos. Improved spectral convergence rates for graph laplacians on ε -graphs and k-nn graphs. *Applied and Computational Harmonic Analysis*, 60:123–175, 2022.
- [40] Mikhail Belkin and Partha Niyogi. Towards a theoretical foundation for laplacian-based manifold methods. *Journal of Computer and System Sciences*, 74(8):1289–1308, 2008.
- [41] David B Dunson, Hau-Tieng Wu, and Nan Wu. Spectral convergence of graph laplacian and heat kernel reconstruction in l^∞ from random samples. *Applied and Computational Harmonic Analysis*, 55:282–336, 2021.
- [42] Yuchen Xie, Jeffrey Ho, and Baba C Vemuri. Multiple atlas construction from a heterogeneous brain mr image collection. *IEEE transactions on medical imaging*, 32(3):628–635, 2013.
- [43] Zhirong Wu, Shuran Song, Aditya Khosla, Fisher Yu, Linguang Zhang, Xiaoou Tang, and Jianxiong Xiao. 3d shapenets: A deep representation for volumetric shapes. In *Proceedings of the IEEE conference on computer vision and pattern recognition*, pages 1912–1920, 2015.
- [44] Tomas Mikolov, Ilya Sutskever, Kai Chen, Greg S Corrado, and Jeff Dean. Distributed representations of words and phrases and their compositionality. *Advances in neural information processing systems*, 26, 2013.
- [45] Zhilin Yang, William Cohen, and Ruslan Salakhudinov. Revisiting semi-supervised learning with graph embeddings. In *International conference on machine learning*, pages 40–48. PMLR, 2016.
- [46] Oleksandr Shchur, Maximilian Mumme, Aleksandar Bojchevski, and Stephan Günnemann. Pitfalls of graph neural network evaluation. *arXiv preprint arXiv:1811.05868*, 2018.
- [47] Oleg Platonov, Denis Kuznedelev, Michael Diskin, Artem Babenko, and Liudmila Prokhorenkova. A critical look at the evaluation of gnns under heterophily: Are we really making progress? *arXiv preprint arXiv:2302.11640*, 2023.
- [48] Qiang Du, Vance Faber, and Max Gunzburger. Centroidal voronoi tessellations: Applications and algorithms. *SIAM review*, 41(4):637–676, 1999.
- [49] Nicolás García Trillos, Moritz Gerlach, Matthias Hein, and Dejan Slepčev. Error estimates for spectral convergence of the graph laplacian on random geometric graphs toward the laplace–beltrami operator. *Foundations of Computational Mathematics*, 20(4):827–887, 2020.
- [50] Ulrike Von Luxburg, Mikhail Belkin, and Olivier Bousquet. Consistency of spectral clustering. *The Annals of Statistics*, pages 555–586, 2008.
- [51] Wolfgang Arendt, Robin Nittka, Wolfgang Peter, and Frank Steiner. Weyl’s law: Spectral properties of the laplacian in mathematics and physics. *Mathematical analysis of evolution, information, and complexity*, pages 1–71, 2009.
- [52] Yiqian Shi and Bin Xu. Gradient estimate of an eigenfunction on a compact riemannian manifold without boundary. *Annals of Global Analysis and Geometry*, 38:21–26, 2010.
- [53] LawrenceCraig Evans. *Measure theory and fine properties of functions*. Routledge, 2018.
- [54] Luana Ruiz, Luiz Chamon, and Alejandro Ribeiro. Graphon neural networks and the transferability of graph neural networks. *Advances in Neural Information Processing Systems*, 33:1702–1712, 2020.
- [55] Sohir Maskey, Ron Levie, and Gitta Kutyniok. Transferability of graph neural networks: an extended graphon approach. *Applied and Computational Harmonic Analysis*, 63:48–83, 2023.

- [56] Nicolas Keriven, Alberto Bietti, and Samuel Vaiter. Convergence and stability of graph convolutional networks on large random graphs. *Advances in Neural Information Processing Systems*, 33:21512–21523, 2020.
- [57] Alejandro Parada-Mayorga, Zhiyang Wang, and Alejandro Ribeiro. Graphon pooling for reducing dimensionality of signals and convolutional operators on graphs. *IEEE Transactions on Signal Processing*, 2023.
- [58] László Lovász. *Large networks and graph limits*, volume 60. American Mathematical Soc., 2012.
- [59] Juan Cervino, Luana Ruiz, and Alejandro Ribeiro. Learning by transference: Training graph neural networks on growing graphs. *IEEE Transactions on Signal Processing*, 71:233–247, 2023.
- [60] Ron Levie, Wei Huang, Lorenzo Bucci, Michael Bronstein, and Gitta Kutyniok. Transferability of spectral graph convolutional neural networks. *Journal of Machine Learning Research*, 22(272):1–59, 2021.
- [61] Thien Le and Stefanie Jegelka. Limits, approximation and size transferability for gnns on sparse graphs via graphops. *Advances in Neural Information Processing Systems*, 36, 2024.
- [62] Jaekoo Lee, Hyunjae Kim, Jongsun Lee, and Sungroh Yoon. Transfer learning for deep learning on graph-structured data. In *Proceedings of the AAAI Conference on Artificial Intelligence*, volume 31, 2017.
- [63] Qi Zhu, Carl Yang, Yidan Xu, Haonan Wang, Chao Zhang, and Jiawei Han. Transfer learning of graph neural networks with ego-graph information maximization. *Advances in Neural Information Processing Systems*, 34:1766–1779, 2021.
- [64] Jiashu He, Charilaos I Kanatsoulis, and Alejandro Ribeiro. Network alignment with transferable graph autoencoders. *arXiv preprint arXiv:2310.03272*, 2023.

Contents

1	Introduction	1
2	Related works	2
2.1	Generalization bounds of GNNs	2
2.2	Neural networks on manifolds	3
3	Preliminaries	3
3.1	Graph neural networks	3
3.2	Manifold neural networks	4
4	Generalization analysis of GNNs based on manifold	5
4.1	Manifold label prediction via node label prediction	5
4.2	Manifold classification via graph classification	7
5	Experiments	7
6	Conclusion	10
A	Induced manifold signals	16
B	Convergence of GNN to MNN	16
C	Local Lipschitz continuity of MNNs	19
D	Proof of Theorem 1	21
E	Proof of Theorem 2	23
F	Experiment details and further experiments	24
F.1	ModelNet10 and ModelNet40 graph classificationtasks	24
F.2	Node classification training details and datasets	25
F.2.1	Arxiv dataset	25
F.2.2	Cora dataset	25
F.2.3	CiteSeer dataset	26
F.2.4	PubMed dataset	26
F.2.5	Coauthors CS dataset	27
F.2.6	Coauthors Physics dataset	28
F.2.7	Heterophilous Amazon ratings dataset	28
F.2.8	Heterophilous Roman Empire dataset	29
G	Further references	32

A Induced manifold signals

The graph signal attached to this constructed graph \mathbf{G} can be seen as the discretization of the continuous function over the manifold. Suppose $f \in L^2(\mathcal{M})$, the graph signal \mathbf{x}_N is composed of discrete data values of the function f evaluated at X_N , i.e. $[\mathbf{x}_N]_i = f(x_i)$ for $i = 1, 2, \dots, N$. With a sampling operator $\mathbf{P}_N : L^2(\mathcal{M}) \rightarrow L^2(X_N)$, the discretization can be written as

$$\mathbf{x}_N = \mathbf{P}_N f. \quad (20)$$

Let $\{V_i\}_{i=1}^N$ be the Voronoi decomposition [48] of \mathcal{M} with respect to X_N with $V_i \subset B_r(x_i)$ and $\text{vol}(V_i) = \mu_i = 1/N$, where $B_r(x_i)$ denoted the closed metric ball of radius r centered at $x_i \in \mathcal{M}$. The Voronoi decomposition can be explicitly denoted as

$$V_i = \{x \in \mathcal{M} : \text{dist}(x_i, x) \leq \text{dist}(x_j, x), j = 1, 2, \dots, i-1, i+1, \dots, N\}, \quad (21)$$

where dist represents the curvature distance between two points on the manifold [37]. The radius of V_i can be bounded as $r \sim (\log N/N)^{1/d}$ [49].

The manifold function induced by the graph signal \mathbf{x}_N over the sampled graph \mathbf{G} is defined by

$$(\mathbf{I}_N \mathbf{x}_N)(x) = \sum_{i=1}^N [\mathbf{x}]_i \mathbb{1}_{x \in V_i}, \text{ for all } x \in \mathcal{M} \quad (22)$$

where we denote $\mathbf{I}_N : L^2(X_N) \rightarrow L^2(\mathcal{M})$ as the inducing operator.

B Convergence of GNN to MNN

The convergence of GNN on sampled graphs to MNN provides the support for the generalization analysis.

Proposition 1. *Let $\mathcal{M} \subset \mathbb{R}^M$ be an embedded manifold with weighted Laplace operator \mathcal{L}_ρ and a bandlimited manifold signal f . Graph \mathbf{G}_N is constructed based on a set of N i.i.d. randomly sampled points $X_N = \{x_1, x_2, \dots, x_N\}$ according to measure μ over \mathcal{M} . A graph signal \mathbf{x} is the sampled manifold function values at X_N . The graph Laplacian \mathbf{L}_N is calculated based on (8) or (9) with ϵ as the graph parameter. Let $\Phi(\mathbf{H}, \mathcal{L}_\rho, \cdot)$ be a MNN on \mathcal{M} (7) with L layers and F features in each layer. Let $\Phi_{\mathbf{G}}(\mathbf{H}, \mathbf{L}_N, \cdot)$ be the GNN with the same architecture applied to the graph \mathbf{G}_N . Then, with the filters as low-pass and nonlinearities as normalized Lipschitz continuous, it holds in probability at least $1 - \delta$ that*

$$\frac{1}{N} \sum_{i=1}^N \|\Phi_{\mathbf{G}}(\mathbf{H}^*, \mathbf{L}_N, \mathbf{x}) - \mathbf{P}_N \Phi(\mathbf{H}^*, \mathcal{L}_\rho, \mathbf{I}_N \mathbf{x})\|_2 \leq LF^{L-1} \left(C_1 \epsilon + C_2 \sqrt{\frac{\log(1/\delta)}{N}} \right) \quad (23)$$

where C_1, C_2 are constants defined in the following proof.

Proposition 2. [35, Proposition 2, Proposition 4] *Let $\mathcal{M} \subset \mathbb{R}^M$ be equipped with Laplace operator \mathcal{L}_ρ , whose eigendecomposition is given by $\{\lambda_i, \phi_i\}_{i=1}^\infty$. Let \mathbf{L}_N be the discrete graph Laplacian of graph weights defined as (8) (or (9)), with spectrum $\{\lambda_{i,N}, \phi_{i,N}\}_{i=1}^N$. Fix $K \in \mathbb{N}^+$ and assume that $\epsilon = \epsilon(N) \geq (\log(C/\delta)/N)^{1/(d+4)}$ (or $\epsilon = \epsilon(N) \geq (\log(CN/\delta)/N)^{1/(d+4)}$). Then, with probability at least $1 - \delta$, we have*

$$|\lambda_i - \lambda_{i,N}| \leq C_{\mathcal{M},1} \lambda_i \epsilon, \quad \|a_i \phi_{i,N} - \phi_i\| \leq C_{\mathcal{M},2} \frac{\lambda_i}{\theta_i} \epsilon, \quad (24)$$

with $a_i \in \{-1, 1\}$ for all $i < K$ and θ the eigengap of \mathcal{L} , i.e., $\theta_i = \min\{\lambda_i - \lambda_{i-1}, \lambda_{i+1} - \lambda_i\}$. The constants $C_{\mathcal{M},1}, C_{\mathcal{M},2}$ depend on d and the volume of \mathcal{M} .

Proof. The inner product of signals $f, g \in L^2(\mathcal{M})$ is defined as

$$\langle f, g \rangle_{\mathcal{M}} = \int_{\mathcal{M}} f(x)g(x) d\mu(x), \quad (25)$$

where $d\mu(x)$ is the volume element with respect to the measure μ over \mathcal{M} . Similarly, the norm of the manifold signal f is

$$\|f\|_{\mathcal{M}}^2 = \langle f, f \rangle_{\mathcal{M}}. \quad (26)$$

Because $\{x_1, x_2, \dots, x_N\}$ is a set of randomly sampled points from \mathcal{M} , based on Theorem 19 in [50] we can claim that

$$|\langle \mathbf{P}_N f, \phi_i \rangle - \langle f, \phi_i \rangle_{\mathcal{M}}| = O\left(\sqrt{\frac{\log(1/\delta)}{N}}\right). \quad (27)$$

This also indicates that

$$|\|\mathbf{P}_N f\|^2 - \|f\|_{\mathcal{M}}^2| = O\left(\sqrt{\frac{\log(1/\delta)}{N}}\right), \quad (28)$$

which indicates $\|\mathbf{P}_N f\| = \|f\|_{\mathcal{M}} + O((\log(1/\delta)/N)^{1/4})$. We suppose that the input manifold signal is λ_M -bandlimited with M spectral components. We first write out the filter representation as

$$\|\mathbf{h}(\mathbf{L}_N)\mathbf{P}_N f - \mathbf{P}_N \mathbf{h}(\mathcal{L}_\rho)f\| \leq \left\| \sum_{i=1}^N \hat{h}(\lambda_{i,N}) \langle \mathbf{P}_N f, \phi_{i,N} \rangle \phi_{i,N} - \sum_{i=1}^M \hat{h}(\lambda_i) \langle f, \phi_i \rangle_{\mathcal{M}} \mathbf{P}_N \phi_i \right\| \quad (29)$$

$$\leq \left\| \sum_{i=1}^M \hat{h}(\lambda_{i,N}) \langle \mathbf{P}_N f, \phi_{i,N} \rangle \phi_{i,N} - \sum_{i=1}^M \hat{h}(\lambda_i) \langle \mathbf{P}_N f, \phi_i \rangle_{\mathcal{M}} \phi_i + \sum_{i=M+1}^N \hat{h}(\lambda_{i,N}) \langle \mathbf{P}_N f, \phi_{i,N} \rangle \phi_{i,N} \right\| \quad (30)$$

$$\leq \left\| \sum_{i=1}^M \hat{h}(\lambda_{i,N}) \langle \mathbf{P}_N f, \phi_{i,N} \rangle \phi_{i,N} - \sum_{i=1}^M \hat{h}(\lambda_i) \langle \mathbf{P}_N f, \phi_i \rangle_{\mathcal{M}} \phi_i \right\| + \left\| \sum_{i=M+1}^N \hat{h}(\lambda_{i,N}) \langle \mathbf{P}_N f, \phi_{i,N} \rangle \phi_{i,N} \right\| \quad (31)$$

The first part of (31) can be decomposed with the triangle inequality as

$$\begin{aligned} & \left\| \sum_{i=1}^M \hat{h}(\lambda_{i,N}) \langle \mathbf{P}_N f, \phi_{i,N} \rangle \phi_{i,N} - \sum_{i=1}^M \hat{h}(\lambda_i) \langle f, \phi_i \rangle_{\mathcal{M}} \mathbf{P}_N \phi_i \right\| \\ & \leq \left\| \sum_{i=1}^M (\hat{h}(\lambda_{i,N}) - \hat{h}(\lambda_i)) \langle \mathbf{P}_N f, \phi_{i,N} \rangle \phi_{i,N} \right\| + \left\| \sum_{i=1}^M \hat{h}(\lambda_i) (\langle \mathbf{P}_N f, \phi_{i,N} \rangle \phi_{i,N} - \langle f, \phi_i \rangle_{\mathcal{M}} \mathbf{P}_N \phi_i) \right\|. \end{aligned} \quad (32)$$

In equation (32), the first part relies on the difference of eigenvalues and the second part depends on the eigenvector difference. The first term in (32) is bounded with Cauchy-Schwartz inequality as

$$\left\| \sum_{i=1}^M (\hat{h}(\lambda_{i,N}) - \hat{h}(\lambda_i)) \langle \mathbf{P}_N f, \phi_{i,N} \rangle \phi_{i,N} \right\| \leq \sum_{i=1}^M |\hat{h}(\lambda_{i,N}) - \hat{h}(\lambda_i)| |\langle \mathbf{P}_N f, \phi_{i,N} \rangle| \quad (33)$$

$$\leq \|\mathbf{P}_N f\| \sum_{i=1}^M C_{\mathcal{M},1} \epsilon \lambda_i^{-d} \leq \|\mathbf{P}_N f\| C_{\mathcal{M},1} \epsilon \sum_{i=1}^M i^{-2} \quad (34)$$

$$\leq \left(\|f\|_{\mathcal{M}} + \left(\frac{\log(1/\delta)}{N} \right)^{\frac{1}{4}} \right) C_{\mathcal{M},1} \epsilon \frac{\pi^2}{6} := A_1(N) \quad (35)$$

In (34), we implement Weyl's law [51] which indicates that eigenvalues of Laplace operator scales with the order $\lambda_i \sim i^{2/d}$. The last inequality comes from the fact that $\sum_{i=1}^{\infty} i^{-2} = \frac{\pi^2}{6}$. The second term in (32) can be bounded with the triangle inequality as

$$\begin{aligned} & \left\| \sum_{i=1}^M \hat{h}(\lambda_i) (\langle \mathbf{P}_N f, \phi_{i,N} \rangle \phi_{i,N} - \langle f, \phi_i \rangle_{\mathcal{M}} \mathbf{P}_N \phi_i) \right\| \\ & \leq \left\| \sum_{i=1}^M \hat{h}(\lambda_i) (\langle \mathbf{P}_N f, \phi_{i,N} \rangle \phi_{i,N} - \langle \mathbf{P}_N f, \phi_{i,N} \rangle \mathbf{P}_N \phi_i) \right\| \\ & \quad + \left\| \sum_{i=1}^M \hat{h}(\lambda_i) (\langle \mathbf{P}_N f, \phi_{i,N} \rangle \mathbf{P}_N \phi_i - \langle f, \phi_i \rangle_{\mathcal{M}} \mathbf{P}_N \phi_i) \right\| \end{aligned} \quad (36)$$

The first term in (36) can be bounded with inserting the eigenfunction convergence result in Proposition 2 as

$$\begin{aligned} & \left\| \sum_{i=1}^M \hat{h}(\lambda_i) (\langle \mathbf{P}_N f, \phi_{i,N} \rangle \phi_{i,N} - \langle \mathbf{P}_N f, \phi_{i,N} \rangle_{\mathcal{M}} \mathbf{P}_N \phi_i) \right\| \\ & \leq \sum_{i=1}^M \left| \hat{h}(\lambda_i) \right| \|\mathbf{P}_N f\| \|\phi_{i,N} - \mathbf{P}_N \phi_i\| \end{aligned} \quad (37)$$

$$\leq \sum_{i=1}^M (\lambda_i^{-d}) \frac{C_{\mathcal{M},2}\epsilon}{\theta_i} \left(\|f\|_{\mathcal{M}} + \left(\frac{\log(1/\delta)}{N} \right)^{\frac{1}{4}} \right) \quad (38)$$

$$\leq C_{\mathcal{M},2}\epsilon \frac{\pi^2}{6} \max_{i=1,\dots,M} \theta_i^{-1} \left(\|f\|_{\mathcal{M}} + \left(\frac{\log(1/\delta)}{N} \right)^{\frac{1}{4}} \right) \quad (39)$$

$$:= A_2(M, N). \quad (40)$$

Considering the low-pass filter assumption, the second term in (36) can be written as

$$\begin{aligned} & \left\| \sum_{i=1}^M \hat{h}(\lambda_{i,N}) (\langle \mathbf{P}_N f, \phi_{i,N} \rangle \mathbf{P}_N \phi_i - \langle f, \phi_i \rangle_{\mathcal{M}} \mathbf{P}_N \phi_i) \right\| \\ & \leq \sum_{i=1}^M \left| \hat{h}(\lambda_{i,N}) \right| |\langle \mathbf{P}_N f, \phi_{i,N} \rangle - \langle f, \phi_i \rangle_{\mathcal{M}}| \|\mathbf{P}_N \phi_i\| \end{aligned} \quad (41)$$

$$\leq \sum_{i=1}^M (\lambda_i^{-d}) \sqrt{\frac{\log(1/\delta)}{N}} \left(1 + \left(\frac{\log(1/\delta)}{N} \right)^{\frac{1}{4}} \right) \quad (42)$$

$$\leq \frac{\pi^2}{6} \sqrt{\frac{\log(1/\delta)}{N}} \left(1 + \left(\frac{\log(1/\delta)}{N} \right)^{\frac{1}{4}} \right) := A_3(N) \quad (43)$$

The second term in (31) can be bounded with the eigenvalue difference bound in Proposition 2 as

$$\left\| \sum_{i=M+1}^N \hat{h}(\lambda_{i,N}) \langle \mathbf{P}_N f, \phi_{i,N} \rangle \phi_{i,N} \right\| \leq \sum_{i=M+1}^N (\lambda_{i,N}^{-d}) \left(\|f\|_{\mathcal{M}} + \left(\frac{\log(1/\delta)}{N} \right)^{\frac{1}{4}} \right) \quad (44)$$

$$\leq \sum_{i=M+1}^{\infty} (\lambda_{i,N}^{-d}) \|f\|_{\mathcal{M}} \quad (45)$$

$$\leq (1 + C_{\mathcal{M},1}\epsilon)^{-d} \sum_{i=M+1}^{\infty} (\lambda_i^{-d}) \|f\|_{\mathcal{M}} \quad (46)$$

$$\leq M^{-1} \|f\|_{\mathcal{M}} := A_4(M). \quad (47)$$

We note that the bound is made up by terms $A_1(N) + A_2(M, N) + A_3(N) + A_4(M)$, related to the bandwidth of manifold signal M and the number of sampled points N . This makes the bound scale with the order

$$\|\mathbf{h}(\mathbf{L}_N) \mathbf{P}_N f - \mathbf{P}_N \mathbf{h}(\mathcal{L}_\rho) f\| \leq C'_1 \epsilon + C'_2 \epsilon \theta_M^{-1} + C'_3 \sqrt{\frac{\log(1/\delta)}{N}} + C'_4 M^{-1}, \quad (48)$$

with $C'_1 = C_{\mathcal{M},1} \frac{\pi^2}{6} \|f\|_{\mathcal{M}}$, $C'_2 = C_{\mathcal{M},2} \frac{\pi^2}{6}$, $C'_3 = \frac{\pi^2}{6}$ and $C'_4 = \|f\|_{\mathcal{M}}$. As N goes to infinity, for every $\delta > 0$, there exists some M_0 , such that for all $M > M_0$ it holds that $A_4(M) \leq \delta/2$. There also exists n_0 , such that for all $N > n_0$, it holds that $A_1(N) + A_2(M_0, N) + A_3(N) \leq \delta/2$. We can conclude that the summations converge as N goes to infinity. We see M large enough to have $M^{-1} \leq \delta'$, which makes the eigengap θ_M also bounded by some constant. We combine the first two terms as

$$\|\mathbf{h}(\mathbf{L}_N) \mathbf{P}_N f - \mathbf{P}_N \mathbf{h}(\mathcal{L}_\rho) f\| \leq C_1 \epsilon + C_2 \sqrt{\frac{\log(1/\delta)}{N}}, \quad (49)$$

with $C_1 = C'_1 + C'_2 \theta_{\delta'-1}^{-1}$ and $C_2 = C'_3$. To bound the output difference of MNNs, we need to write in the form of features of the final layer

$$\|\Phi_{\mathbf{G}}(\mathbf{H}, \mathbf{L}_N, \mathbf{P}_N f) - \mathbf{P}_N \Phi(\mathbf{H}, \mathcal{L}_\rho, f)\| = \left\| \sum_{q=1}^F \mathbf{x}_{n,L}^q - \sum_{q=1}^F \mathbf{P}_N f_L^q \right\| \leq \sum_{q=1}^F \|\mathbf{x}_{n,L}^q - \mathbf{P}_N f_L^q\|. \quad (50)$$

By inserting the definitions, we have

$$\|\mathbf{x}_{n,l}^p - \mathbf{P}_N f_l^p\| = \left\| \sigma \left(\sum_{q=1}^F \mathbf{h}_l^{pq}(\mathbf{L}_N) \mathbf{x}_{n,l-1}^q \right) - \mathbf{P}_N \sigma \left(\sum_{q=1}^F \mathbf{h}_l^{pq}(\mathcal{L}_\rho) f_{l-1}^q \right) \right\| \quad (51)$$

with $\mathbf{x}_{n,0} = \mathbf{P}_N f$ as the input of the first layer. With a normalized point-wise Lipschitz nonlinearity, we have

$$\|\mathbf{x}_{n,l}^p - \mathbf{P}_N f_l^p\| \leq \left\| \sum_{q=1}^F \mathbf{h}_l^{pq}(\mathbf{L}_N) \mathbf{x}_{n,l-1}^q - \mathbf{P}_N \sum_{q=1}^F \mathbf{h}_l^{pq}(\mathcal{L}_\rho) f_{l-1}^q \right\| \quad (52)$$

$$\leq \sum_{q=1}^F \left\| \mathbf{h}_l^{pq}(\mathbf{L}_N) \mathbf{x}_{n,l-1}^q - \mathbf{P}_N \mathbf{h}_l^{pq}(\mathcal{L}_\rho) f_{l-1}^q \right\| \quad (53)$$

The difference can be further decomposed as

$$\begin{aligned} & \|\mathbf{h}_l^{pq}(\mathbf{L}_N) \mathbf{x}_{n,l-1}^q - \mathbf{P}_N \mathbf{h}_l^{pq}(\mathcal{L}_\rho) f_{l-1}^q\| \\ & \leq \|\mathbf{h}_l^{pq}(\mathbf{L}_N) \mathbf{x}_{n,l-1}^q - \mathbf{h}_l^{pq}(\mathbf{L}_N) \mathbf{P}_N f_{l-1}^q + \mathbf{h}_l^{pq}(\mathbf{L}_N) \mathbf{P}_N f_{l-1}^q - \mathbf{P}_N \mathbf{h}_l^{pq}(\mathcal{L}_\rho) f_{l-1}^q\| \end{aligned} \quad (54)$$

$$\leq \left\| \mathbf{h}_l^{pq}(\mathbf{L}_N) \mathbf{x}_{n,l-1}^q - \mathbf{h}_l^{pq}(\mathbf{L}_N) \mathbf{P}_N f_{l-1}^q \right\| + \left\| \mathbf{h}_l^{pq}(\mathbf{L}_N) \mathbf{P}_N f_{l-1}^q - \mathbf{P}_N \mathbf{h}_l^{pq}(\mathcal{L}_\rho) f_{l-1}^q \right\| \quad (55)$$

The second term can be bounded with (48) and we denote the bound as Δ_N for simplicity. The first term can be decomposed by Cauchy-Schwartz inequality and non-amplifying of the filter functions as

$$\left\| \mathbf{x}_{n,l}^p - \mathbf{P}_N f_l^p \right\| \leq \sum_{q=1}^F \Delta_N \|\mathbf{x}_{n,l-1}^q\| + \sum_{q=1}^F \|\mathbf{x}_{l-1}^q - \mathbf{P}_N f_{l-1}^q\|. \quad (56)$$

To solve this recursion, we need to compute the bound for $\|\mathbf{x}_l^p\|$. By normalized Lipschitz continuity of σ and the fact that $\sigma(0) = 0$, we can get

$$\|\mathbf{x}_l^p\| \leq \left\| \sum_{q=1}^F \mathbf{h}_l^{pq}(\mathbf{L}_N) \mathbf{x}_{l-1}^q \right\| \leq \sum_{q=1}^F \|\mathbf{h}_l^{pq}(\mathbf{L}_N)\| \|\mathbf{x}_{l-1}^q\| \leq \sum_{q=1}^F \|\mathbf{x}_{l-1}^q\| \leq F^{l-1} \|\mathbf{x}\|. \quad (57)$$

Insert this conclusion back to solve the recursion, we can get

$$\left\| \mathbf{x}_{n,l}^p - \mathbf{P}_N f_l^p \right\| \leq l F^{l-1} \Delta_N \|\mathbf{x}\|. \quad (58)$$

Replace l with L we can obtain

$$\|\Phi_{\mathbf{G}}(\mathbf{H}, \mathbf{L}_N, \mathbf{P}_N f) - \mathbf{P}_N \Phi(\mathbf{H}, \mathcal{L}_\rho, f)\| \leq L F^{L-1} \Delta_N, \quad (59)$$

when the input graph signal is normalized. By replacing $f = \mathbf{I}_N \mathbf{x}$, we can conclude the proof. \square

C Local Lipschitz continuity of MNNs

We propose that the outputs of MNN defined in (7) are locally Lipschitz continuous within a certain area, which is stated explicitly as follows.

Proposition 3. (Local Lipschitz continuity of MNNs) *Let MNN be L layers with F features in each layer, suppose the manifold filters are nonamplifying with $|\hat{h}(\lambda)| \leq 1$ and the nonlinearities normalized Lipschitz continuous, then there exists a constant C such that*

$$|\Phi(\mathbf{H}, \mathcal{L}_\rho, f)(x) - \Phi(\mathbf{H}, \mathcal{L}_\rho, f)(y)| \leq F^L C' \|x - y\|, \quad \text{for all } x, y \in B_r(\mathcal{M}), \quad (60)$$

where $B_r(\mathcal{M})$ is a ball with radius r over \mathcal{M} .

Proof. The output of MNN can be written explicitly as

$$|\Phi(\mathbf{H}, \mathcal{L}_\rho, f)(x) - \Phi(\mathbf{H}, \mathcal{L}_\rho, f)(y)| = \left| \sigma \left(\sum_{q=1}^F \mathbf{h}_L^q(\mathcal{L}_\rho) f_{L-1}^q(x) \right) - \sigma \left(\sum_{q=1}^F \mathbf{h}_L^q(\mathcal{L}_\rho) f_{L-1}^q(y) \right) \right| \quad (61)$$

$$\leq \left| \sum_{q=1}^F \mathbf{h}_L^q(\mathcal{L}_\rho) f_{L-1}^q(x) - \sum_{q=1}^F \mathbf{h}_L^q(\mathcal{L}_\rho) f_{L-1}^q(y) \right| \leq F |f_{L-1}^q(x) - f_{L-1}^q(y)|. \quad (62)$$

We have $f_{L-1}^q(x) = \sigma \left(\sum_{p=1}^F \mathbf{h}_{L-1}^p f_{L-2}^p(x) \right)$. The process can be repeated recursively, and finally, we can have

$$|\Phi(\mathbf{H}, \mathcal{L}_\rho, f)(x) - \Phi(\mathbf{H}, \mathcal{L}_\rho, f)(y)| \leq F^L |f(x) - f(y)|. \quad (63)$$

With f as a λ -bandlimited manifold signal, we suppose it possesses M spectral components. The gradient can be bounded according to [52] as

$$\|\nabla f\|_\infty \leq C \sum_{\lambda_i \leq \lambda} \lambda_i \|\phi_i\|_\infty \quad (64)$$

From Theorem 4.5 in [53], f is locally Lipschitz continuous as

$$|f(x) - f(y)| \leq C' \|x - y\|, \quad \text{with } x, y \in B_r(\mathcal{M}), \quad (65)$$

where $B_r(\mathcal{M})$ is a closed ball with radius r .

Combining the above, we have the continuity of the output of MNN as

$$|\Phi(\mathbf{H}, \mathcal{L}_\rho, f)(x) - \Phi(\mathbf{H}, \mathcal{L}_\rho, f)(y)| \leq F^L C' \|x - y\|, \quad \text{with } x, y \in B_r(\mathcal{M}), \quad (66)$$

which concludes the proof. \square

D Proof of Theorem 1

Proof. To analyze the difference between the empirical risk and statistical risk, we introduce an intermediate term which is the induced version of the sampled MNN output. We define \mathbf{I}_N as the inducing operator based on the Voronoi decomposition $\{V_i\}_{i=1}^N$ defined in (21). This intermediate term is written explicitly as

$$\bar{\Phi}(\mathbf{H}, \mathcal{L}_\rho, f)(x) = \mathbf{I}_N \mathbf{P}_N \Phi(\mathbf{H}, \mathcal{L}_\rho, f)(x) = \sum_{i=1}^N \Phi(\mathbf{H}, \mathcal{L}_\rho, f)(x_i) \mathbb{1}_{x \in V_i}, \text{ for all } x \in \mathcal{M}, \quad (67)$$

where $x_i \in X_N$ are sampled points from the manifold.

Suppose $\mathbf{H}^* \in \arg \min_{\mathbf{H} \in \mathcal{H}} R_{\mathcal{M}}(\mathbf{H})$, we have

$$GA = \min_{\mathbf{H} \in \mathcal{H}} R_{\mathbf{G}}(\mathbf{H}) - \min_{\mathbf{H} \in \mathcal{H}} R_{\mathcal{M}}(\mathbf{H}) \leq R_{\mathbf{G}}(\mathbf{H}^*) - R_{\mathcal{M}}(\mathbf{H}^*) \quad (68)$$

The difference between $R_{\mathbf{G}}(\mathbf{H}^*)$ and $R_{\mathcal{M}}(\mathbf{H}^*)$ can be decomposed as

$$\begin{aligned} & R_{\mathbf{G}}(\mathbf{H}^*) - R_{\mathcal{M}}(\mathbf{H}^*) \\ &= \frac{1}{N} \sum_{i=1}^N \ell([\Phi_{\mathbf{G}}(\mathbf{H}^*, \mathbf{L}_N, \mathbf{x})]_i, [\mathbf{y}]_i) - \int_{\mathcal{M}} \ell(\Phi(\mathbf{H}^*, \mathcal{L}_\rho, f)(x), g(x)) \mathrm{d}\mu(x) \end{aligned} \quad (69)$$

$$\begin{aligned} &= \frac{1}{N} \sum_{i=1}^N \ell([\Phi_{\mathbf{G}}(\mathbf{H}^*, \mathbf{L}_N, \mathbf{x})]_i, [\mathbf{y}]_i) - \int_{\mathcal{M}} \ell(\bar{\Phi}(\mathbf{H}^*, \mathcal{L}_\rho, f)(x), g(x)) \mathrm{d}\mu(x) \\ &\quad + \int_{\mathcal{M}} \ell(\bar{\Phi}(\mathbf{H}^*, \mathcal{L}_\rho, f)(x), g(x)) \mathrm{d}\mu(x) - \int_{\mathcal{M}} \ell(\Phi(\mathbf{H}^*, \mathcal{L}_\rho, f)(x), g(x)) \mathrm{d}\mu(x) \end{aligned} \quad (70)$$

$$\begin{aligned} &\leq \left| \frac{1}{N} \sum_{i=1}^N \ell([\Phi_{\mathbf{G}}(\mathbf{H}^*, \mathbf{L}_N, \mathbf{x})]_i, [\mathbf{y}]_i) - \int_{\mathcal{M}} \ell(\bar{\Phi}(\mathbf{H}^*, \mathcal{L}_\rho, f)(x), g(x)) \mathrm{d}\mu(x) \right| \\ &\quad + \left| \int_{\mathcal{M}} \ell(\bar{\Phi}(\mathbf{H}^*, \mathcal{L}_\rho, f)(x), g(x)) \mathrm{d}\mu(x) - \int_{\mathcal{M}} \ell(\Phi(\mathbf{H}^*, \mathcal{L}_\rho, f)(x), g(x)) \mathrm{d}\mu(x) \right| \end{aligned} \quad (71)$$

We analyze the two terms in (71) separately, with the first term bounded based on the convergence of GNN to MNN and the second term bounded with the smoothness of manifold functions.

The first term in (71) can be written as

$$\left| \frac{1}{N} \sum_{i=1}^N \ell([\Phi_{\mathbf{G}}(\mathbf{H}^*, \mathbf{L}_N, \mathbf{x})]_i, [\mathbf{y}]_i) - \int_{\mathcal{M}} \ell(\bar{\Phi}(\mathbf{H}^*, \mathcal{L}_\rho, f)(x), g(x)) \mathrm{d}\mu(x) \right| \quad (72)$$

$$= \frac{1}{N} \left| \sum_{i=1}^N \ell([\Phi_{\mathbf{G}}(\mathbf{H}^*, \mathbf{L}_N, \mathbf{x})]_i, [\mathbf{y}]_i) - \sum_{i=1}^N \ell(\Phi(\mathbf{H}^*, \mathcal{L}_\rho, f)(x_i), g(x_i)) \right| \quad (73)$$

$$\leq \frac{1}{N} \sum_{i=1}^N |\ell([\Phi_{\mathbf{G}}(\mathbf{H}^*, \mathbf{L}_N, \mathbf{x})]_i, [\mathbf{y}]_i) - \ell(\Phi(\mathbf{H}^*, \mathcal{L}_\rho, f)(x_i), g(x_i))| \quad (74)$$

$$\leq \frac{1}{N} \sum_{i=1}^N \left| [\Phi_{\mathbf{G}}(\mathbf{H}^*, \mathbf{L}_N, \mathbf{x})]_i - \Phi(\mathbf{H}^*, \mathcal{L}_\rho, f)(x_i) \right| \quad (75)$$

$$\leq \frac{1}{N} \|\Phi_{\mathbf{G}}(\mathbf{H}^*, \mathbf{L}_N, \mathbf{x}) - \mathbf{P}_N \Phi(\mathbf{H}^*, \mathcal{L}_\rho, \mathbf{I}_N \mathbf{x})\|_1 \quad (76)$$

$$\leq \frac{1}{\sqrt{N}} \left(C_1 \epsilon + C_2 \sqrt{\frac{\log(1/\delta)}{N}} \right) \quad (77)$$

From (72) to (73), we use the definition of induced manifold signal defined in (67). We utilize the Lipschitz continuity assumption on loss function from (74) to (75). From (75) to (76), it depends on the fact that \mathbf{x} is a single-entry vector and that $[\mathbf{y}]_i$ is the value sampled from target manifold function

g evaluated on x_i . Finally the bound depends on the convergence of GNN on the sampled graph to the MNN as stated in Proposition 1.

The second term is decomposed as

$$\left| \int_{\mathcal{M}} \ell(\bar{\Phi}(\mathbf{H}^*, \mathcal{L}_\rho, f)(x), g(x)) \, \mathrm{d}\mu(x) - \int_{\mathcal{M}} \ell(\Phi(\mathbf{H}^*, \mathcal{L}_\rho, f)(x), g(x)) \, \mathrm{d}\mu(x) \right| \quad (78)$$

$$\leq \left| \sum_{i=1}^N \int_{V_i} \ell(\bar{\Phi}(\mathbf{H}^*, \mathcal{L}_\rho, f)(x), g(x)) \, \mathbb{1}_{x \in V_i} \, \mathrm{d}\mu(x) - \sum_{i=1}^N \int_{V_i} \ell(\Phi(\mathbf{H}^*, \mathcal{L}_\rho, f)(x), g(x)) \, \mathrm{d}\mu(x) \right| \quad (79)$$

$$\leq \sum_{i=1}^N \int_{V_i} \left| \ell(\bar{\Phi}(\mathbf{H}^*, \mathcal{L}_\rho, f)(x), g(x)) - \ell(\Phi(\mathbf{H}^*, \mathcal{L}_\rho, f)(x), g(x)) \right| \, \mathbb{1}_{x \in V_i} \, \mathrm{d}\mu(x) \quad (80)$$

$$\leq \sum_{i=1}^N \int_{V_i} \left| \bar{\Phi}(\mathbf{H}^*, \mathcal{L}_\rho, f)(x) - \Phi(\mathbf{H}^*, \mathcal{L}_\rho, f)(x) \right| \, \mathbb{1}_{x \in V_i} \, \mathrm{d}\mu(x) \quad (81)$$

$$\leq \sum_{i=1}^N \int_{V_i} \left| \Phi(\mathbf{H}^*, \mathcal{L}_\rho, f)(x_i) - \Phi(\mathbf{H}^*, \mathcal{L}_\rho, f)(x) \right| \, \mathbb{1}_{x \in V_i} \, \mathrm{d}\mu(x) \quad (82)$$

From (78) to (79), it relies on the decomposition of the MNN output over $\{V_i\}_{i=1}^N$. From (80) to (82), we use the Lipschitz continuity of loss function. Proposition 3 indicates that the MNN outputs are Lipschitz continuous within a certain range, which leads to

$$\sum_{i=1}^N \int_{V_i} \left| \Phi(\mathbf{H}^*, \mathcal{L}_\rho, f)(x_i) - \Phi(\mathbf{H}^*, \mathcal{L}_\rho, f)(x) \right| \, \mathbb{1}_{x \in V_i} \, \mathrm{d}\mu(x) \leq F^L C_3 \left(\frac{\log N}{N} \right)^{\frac{1}{d}}. \quad (83)$$

Combining (77) and (83), we can conclude the proof. \square

E Proof of Theorem 2

Proof. Suppose $\mathbf{H}^* \in \arg \min_{\mathbf{H} \in \mathcal{H}} R_{\mathcal{M}}(\mathbf{H})$, we have

$$GA = \min_{\mathbf{H} \in \mathcal{H}} R_{\mathbf{G}}(\mathbf{H}) - \min_{\mathbf{H} \in \mathcal{H}} R_{\mathcal{M}}(\mathbf{H}) \leq R_{\mathbf{G}}(\mathbf{H}^*) - R_{\mathcal{M}}(\mathbf{H}^*) \quad (84)$$

We can write the difference as

$$\begin{aligned} & R_{\mathbf{G}}(\mathbf{H}^*) - R_{\mathcal{M}}(\mathbf{H}^*) \\ &= \sum_{k=1}^K \left(\ell \left(\frac{1}{N} \sum_{i=1}^N [\Phi_{\mathbf{G}}(\mathbf{H}^*, \mathbf{L}_{N,k}, \mathbf{x}_k)]_i, y_k \right) - \ell \left(\int_{\mathcal{M}_k} \Phi(\mathbf{H}^*, \mathcal{L}_{\rho,k}, f_k) d\mu_k(x), y_k \right) \right) \end{aligned} \quad (85)$$

Based on the property of absolute value inequality, we have

$$\begin{aligned} & \ell \left(\frac{1}{N} \sum_{i=1}^N [\Phi_{\mathbf{G}}(\mathbf{H}^*, \mathbf{L}_{N,k}, \mathbf{x}_k)]_i, y_k \right) - \ell \left(\int_{\mathcal{M}_k} \Phi(\mathbf{H}^*, \mathcal{L}_{\rho,k}, f_k) d\mu_k(x), y_k \right) \\ & \leq \left| \frac{1}{N} \sum_{i=1}^N [\Phi_{\mathbf{G}}(\mathbf{H}^*, \mathbf{L}_{N,k}, \mathbf{x}_k)]_i - \int_{\mathcal{M}_k} \Phi(\mathbf{H}^*, \mathcal{L}_{\rho,k}, f_k) d\mu_k(x) \right| \end{aligned} \quad (86)$$

We insert an intermediate term $\Phi(\mathbf{H}^*, \mathcal{L}_{\rho,k}, f_k)(x_i)$ as the value evaluated on the sampled point x_i , which leads to

$$\left| \frac{1}{N} \sum_{i=1}^N [\Phi_{\mathbf{G}}(\mathbf{H}^*, \mathbf{L}_{N,k}, \mathbf{x}_k)]_i - \int_{\mathcal{M}_k} \Phi(\mathbf{H}^*, \mathcal{L}_{\rho,k}, f_k) d\mu_k(x) \right| \quad (87)$$

$$\begin{aligned} & \leq \left| \frac{1}{N} \sum_{i=1}^N [\Phi_{\mathbf{G}}(\mathbf{H}^*, \mathbf{L}_{N,k}, \mathbf{x}_k)]_i - \frac{1}{N} \sum_{i=1}^N \Phi(\mathbf{H}^*, \mathcal{L}_{\rho,k}, f_k)(x_i) \right| + \\ & \quad \left| \frac{1}{N} \sum_{i=1}^N \Phi(\mathbf{H}^*, \mathcal{L}_{\rho,k}, f_k)(x_i) - \int_{\mathcal{M}_k} \Phi(\mathbf{H}^*, \mathcal{L}_{\rho,k}, f_k) d\mu_k(x) \right| \end{aligned} \quad (88)$$

The first term in (88) can be bounded similarly as (76), which is explicitly written as

$$\left| \frac{1}{N} \sum_{i=1}^N [\Phi_{\mathbf{G}}(\mathbf{H}^*, \mathbf{L}_{N,k}, \mathbf{x}_k)]_i - \frac{1}{N} \sum_{i=1}^N \Phi(\mathbf{H}^*, \mathcal{L}_{\rho,k}, f_k)(x_i) \right| \quad (89)$$

$$\leq \frac{1}{N} \|\Phi_{\mathbf{G}}(\mathbf{H}^*, \mathbf{L}_N, \mathbf{x}_k) - \mathbf{P}_N \Phi(\mathbf{H}^*, \mathcal{L}_{\rho}, f_k)\|_1 \quad (90)$$

$$\leq \frac{1}{\sqrt{N}} \|\Phi_{\mathbf{G}}(\mathbf{H}^*, \mathbf{L}_N, \mathbf{x}_k) - \mathbf{P}_N \Phi(\mathbf{H}^*, \mathcal{L}_{\rho}, f_k)\|_2 \quad (91)$$

$$\leq \frac{1}{\sqrt{N}} \left(C_1 \epsilon + C_2 \sqrt{\frac{\log(1/\delta)}{N}} \right) \quad (92)$$

The second term is

$$\left| \frac{1}{N} \sum_{i=1}^N \Phi(\mathbf{H}^*, \mathcal{L}_{\rho,k}, f_k)(x_i) - \int_{\mathcal{M}_k} \Phi(\mathbf{H}^*, \mathcal{L}_{\rho,k}, f_k) d\mu_k(x) \right| \quad (93)$$

$$= \left| \sum_{i=1}^N \int_{V_i} \Phi(\mathbf{H}^*, \mathcal{L}_{\rho,k}, f_k)(x_i) \mathbb{1}_{x \in V_i} d\mu_k(x) - \sum_{i=1}^N \int_{V_i} \Phi(\mathbf{H}^*, \mathcal{L}_{\rho,k}, f_k)(x) d\mu_k(x) \right| \quad (94)$$

$$\leq \sum_{i=1}^N \int_{V_i} |\Phi(\mathbf{H}^*, \mathcal{L}_{\rho,k}, f_k)(x_i) - \Phi(\mathbf{H}^*, \mathcal{L}_{\rho,k}, f_k)(x)| \mathbb{1}_{x \in V_i} d\mu_k(x) \quad (95)$$

$$\leq F^L C_3 \left(\frac{\log N}{N} \right)^{\frac{1}{d}} \quad (96)$$

This depends on the Lipschitz continuity of the output manifold function in Proposition 3. \square

F Experiment details and further experiments

All experiments were done using a *NVIDIA GeForce RTX 3090*, and each set of experiments took at most 10 hours to complete. In total, we run 10 datasets, which amounts for around 100 hours of GPU use. All datasets used in this paper are public, and free to use. They can be downloaded using the *pytorch* package (<https://pytorch-geometric.readthedocs.io/en/latest/modules/datasets.html>), the *ogb* package (<https://ogb.stanford.edu/docs/nodeprop/>) and the Princeton ModelNet project (<https://modelnet.cs.princeton.edu/>). In total, the datasets occupy around 5 gb. However, they do not need to be all stored at the same time, as the experiments that we run can be done in series.

F.1 ModelNet10 and ModelNet40 graph classification tasks

ModelNet10 dataset [43] includes 3,991 meshed CAD models from 10 categories for training and 908 models for testing as Figure 7 shows. ModelNet40 dataset includes 38,400 training and 9,600 testing models as Figure 8 shows. In each model, N points are uniformly randomly selected to construct graphs to approximate the underlying model, such as chairs, tables.

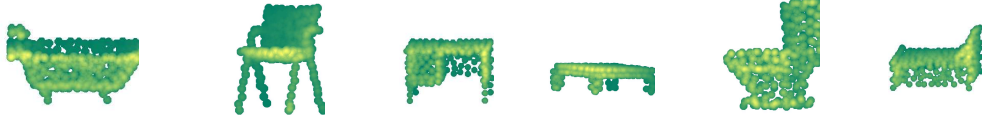


Figure 7: Point cloud models in ModelNet10 with $N = 300$ sampled points in each model, corresponding to bathtub, chair, desk, table, toiler, and bed.

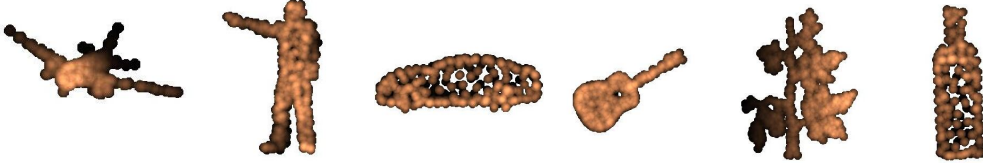
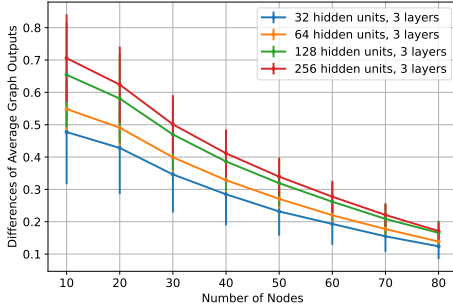
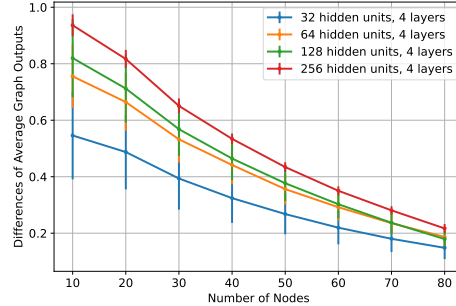


Figure 8: Point cloud models from ModelNet40 with $N = 300$ sampled points in each model, corresponding to airplane, person, car, guitar, plant, and bottle.



(a) Differences of the outputs of 3-layer GNNs.



(b) Differences of the outputs of 4-layer GNNs.

Figure 9: Graph outputs differences of GNNs with different architectures on ModelNet40 dataset.

The weight function of the constructed graph is determined as (8) with $\epsilon = 0.1$. We calculate the Laplacian matrix for each graph as the input graph shift operator. In this experiment, we implement

GNNs with different numbers of layers and hidden units with $K = 5$ filters in each layer. All the GNN architectures are trained by minimizing the cross-entropy loss. We implement an ADAM optimizer with the learning rate set as 0.005 along with the forgetting factors 0.9 and 0.999. We carry out the training for 40 epochs with the size of batches set as 10. We run 5 random dataset partitions and show the average performances and the standard deviation across these partitions.

F.2 Node classification training details and datasets

In this section, we present the results for node classification. In this paragraph we present the common details for all datasets, we will next delve into each specific detail inside the dataset subsection that follows.

Name	Nodes	Edges	Features	Number of Classes	Reference
Arxiv	169,343	1,166,243	128	40	[20, 44]
Cora	2,708	10,556	1,433	7	[45]
CiteSeer	3,327	9,104	3,703	6	[45]
PubMed	19,717	88,648	500	3	[45]
Coauthor Physics	18,333	163,788	6,805	15	[46]
Coauthor CS	34,493	495,924	8,415	5	[46]
Amazon-ratings	24,492	93,050	300	5	[47]
Roman-empire	22,662	32,927	300	18	[47]

Table 2: Details of the datasets considered in the experiments.

In all datasets, we used the graph convolutional layer GCN, and trained for 1000 epochs. For the optimizer, we used AdamW, with using a learning rate of 0.01, and 0 weight decay. We trained using the graph convolutional layer, with a varying number of layers and hidden units. For dropout, we used 0.5. We trained using the cross-entropy loss. In all cases, we trained 2 and 3 layered GNNs.

To compute the linear approximation in the plots, we used the mean squared error estimator of the form

$$\mathbf{y} = s * \log(\mathbf{n}) + p. \quad (97)$$

Where s is the slope, p is the point, and \mathbf{n} is the vector with the nodes in the training set for each experiment. Note that we repeated each experiment for 10 independent runs. In all experiments, we compute the value of s and p that minimize the mean square error over the mean of the experiment runs, and we compute the Pearson correlation index over those values.

Our experiment shows that our bound shows the same rate dependency as the experiments. That is to say, in the logarithmic scale, the generalization gap of GNNs is linear with respect to the logarithm of the number of nodes. In most cases, the Pearson correlation index is above 0.9 in absolute value, which indicates a strong linear relationship. We noticed that the linear relationship changes the slope in the overfitting regime, and in the non-overfitting regime. That is to say, when the GNN is overfitting the training set, the generalization gap decreases at a much slower rate than it does with the GNN does not have the capacity to do so. Therefore, in the case in which the GNN overfits the training set for all nodes when computed s using all the samples in the experiment. On the other hand, when the number of nodes is large enough that the GNN cannot overfit the training set, then we computed the s and p with the nodes in the non overfitting regime.

F.2.1 Arxiv dataset

For this datasets, we trained 2,3,4 layered GNN. We also used a learning rate scheduler ReduceLROnPlateau with mode min, factor 0.5, patience 100 and a minimum learning rate of 0.001.

F.2.2 Cora dataset

For the Cora dataset, we used the standard one, which can be obtained running `torch_geometric.datasets.Planetoid(root='./data',name='Cora')`.

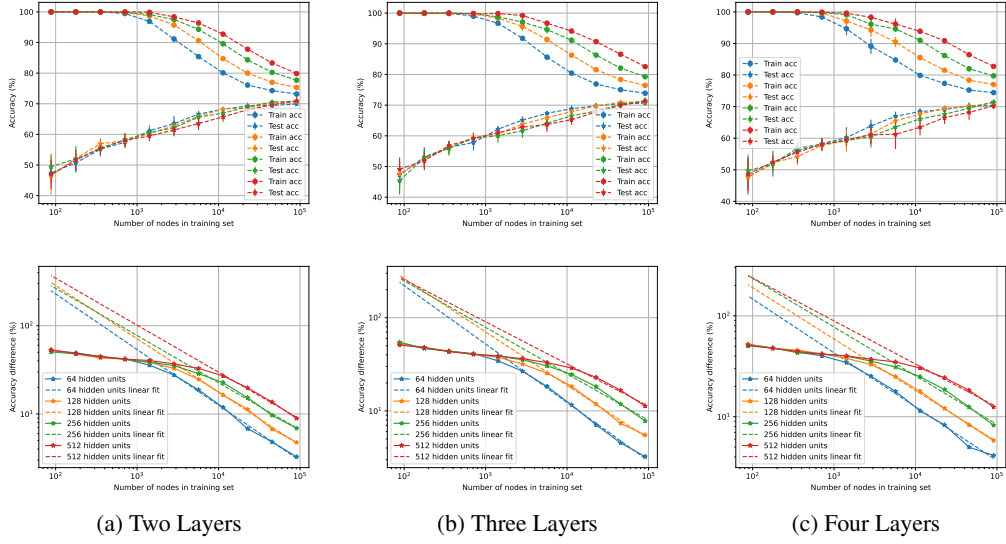


Figure 10: Generalization gap for the OGBN-arxiv dataset on the accuracy as a function of the number of nodes in the training set.

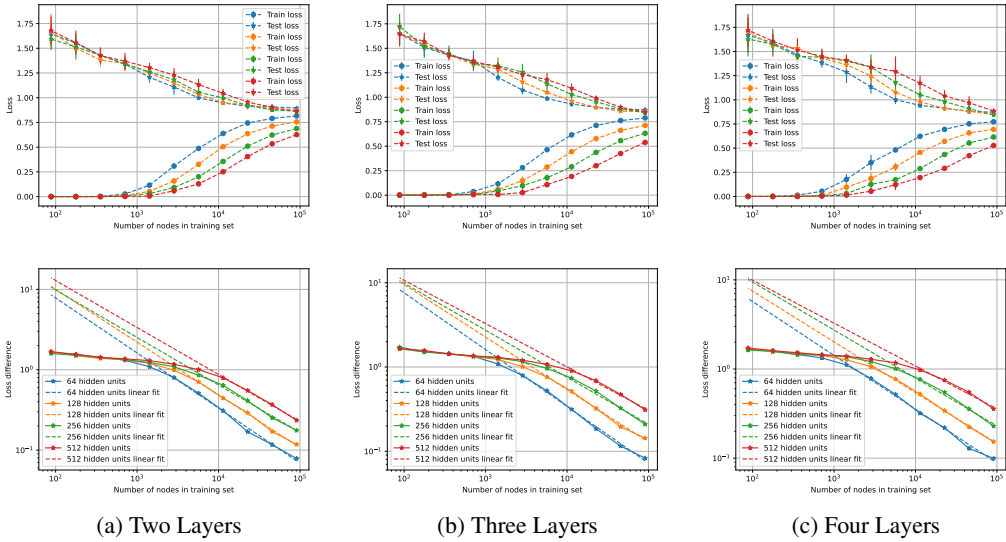


Figure 11: Generalization gap for the OGBN-arxiv dataset on the loss (cross-entropy) as a function of the number of nodes in the training set.

F.2.3 CiteSeer dataset

For the CiteSeer dataset, we used the standard one, which can be obtained running `torch_geometric.datasets.Planetoid(root="./data", name='CiteSeer')`.

F.2.4 PubMed dataset

For the PubMed dataset, we used the standard one, which can be obtained running `torch_geometric.datasets.Planetoid(root="./data", name='PubMed')`.

Type	Lay.	Feat.	Slope	Point	Pearson Correlation Coefficient
Accuracy	2	64	$-6.301e-01$	$3.621e+00$	$-9.980e-01$
Accuracy	2	128	$-6.034e-01$	$3.663e+00$	$-9.985e-01$
Accuracy	2	256	$-5.347e-01$	$3.493e+00$	$-9.952e-01$
Accuracy	2	512	$-5.328e-01$	$3.605e+00$	$-9.975e-01$
Accuracy	3	64	$-6.271e-01$	$3.600e+00$	$-9.987e-01$
Accuracy	3	128	$-5.730e-01$	$3.567e+00$	$-9.970e-01$
Accuracy	3	256	$-4.986e-01$	$3.393e+00$	$-9.910e-01$
Accuracy	3	512	$-4.529e-01$	$3.315e+00$	$-9.934e-01$
Accuracy	4	64	$-5.343e-01$	$3.236e+00$	$-9.971e-01$
Accuracy	4	128	$-5.096e-01$	$3.299e+00$	$-9.987e-01$
Accuracy	4	256	$-4.827e-01$	$3.337e+00$	$-9.920e-01$
Accuracy	4	512	$-4.264e-01$	$3.229e+00$	$-9.927e-01$
Loss	2	64	$-6.853e-01$	$2.265e+00$	$-9.975e-01$
Loss	2	128	$-6.562e-01$	$2.311e+00$	$-9.988e-01$
Loss	2	256	$-5.907e-01$	$2.174e+00$	$-9.968e-01$
Loss	2	512	$-5.848e-01$	$2.280e+00$	$-9.989e-01$
Loss	3	64	$-6.739e-01$	$2.228e+00$	$-9.980e-01$
Loss	3	128	$-6.229e-01$	$2.224e+00$	$-9.976e-01$
Loss	3	256	$-5.581e-01$	$2.111e+00$	$-9.942e-01$
Loss	3	512	$-5.141e-01$	$2.057e+00$	$-9.955e-01$
Loss	4	64	$-6.039e-01$	$1.964e+00$	$-9.980e-01$
Loss	4	128	$-5.701e-01$	$2.014e+00$	$-9.991e-01$
Loss	4	256	$-5.379e-01$	$2.051e+00$	$-9.951e-01$
Loss	4	512	$-4.810e-01$	$1.957e+00$	$-9.937e-01$

Table 3: Details of the linear approximation of the Arxiv Dataset. Note that in this case, we used only the values of the generalization gap whose training error is below 95%.

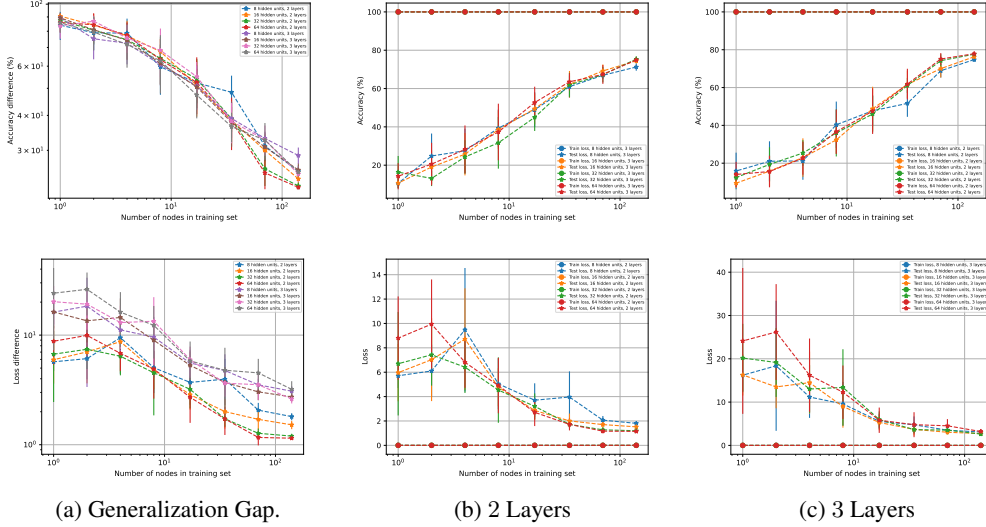


Figure 12: Generalization gap, testing, and training losses with respect to the number of nodes in the Cora dataset. The top row is in accuracy, and the bottom row is the cross-entropy loss.

F.2.5 Coauthors CS dataset

For the CS dataset, we used the standard one, which can be obtained running `torch_geometric.datasets.Coauthor(root="./data", name='CS')`. In this case, given

Type	Lay.	Feat.	Slope	Point	Pearson Correlation Coefficient
Accuracy	2	16	$-2.839e-01$	$2.022e+00$	$-9.803e-01$
Accuracy	2	32	$-2.917e-01$	$2.014e+00$	$-9.690e-01$
Accuracy	2	64	$-3.006e-01$	$2.021e+00$	$-9.686e-01$
Accuracy	3	16	$-2.656e-01$	$1.996e+00$	$-9.891e-01$
Accuracy	3	32	$-2.637e-01$	$2.008e+00$	$-9.679e-01$
Accuracy	3	64	$-2.581e-01$	$1.981e+00$	$-9.870e-01$
Loss	2	16	$-3.631e-01$	$9.406e-01$	$-9.250e-01$
Loss	2	32	$-4.228e-01$	$9.638e-01$	$-9.657e-01$
Loss	2	64	$-4.991e-01$	$1.067e+00$	$-9.776e-01$
Loss	3	16	$-4.131e-01$	$1.276e+00$	$-9.753e-01$
Loss	3	32	$-4.605e-01$	$1.385e+00$	$-9.730e-01$
Loss	3	64	$-4.589e-01$	$1.455e+00$	$-9.756e-01$

Table 4: Details of the linear approximation of the Cora Dataset. Note that in this case we used all the values given that the training accuracy is 100% for all nodes.

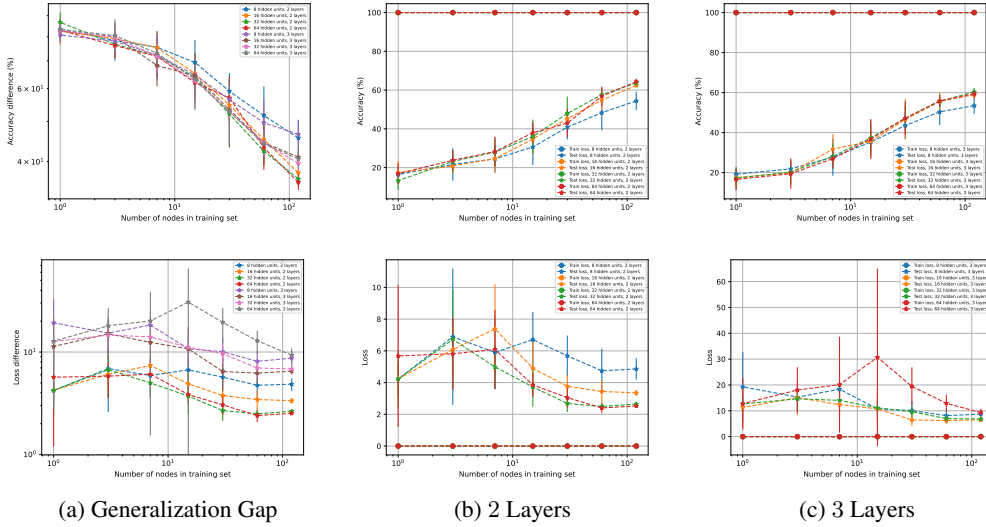


Figure 13: Generalization gap, testing, and training losses with respect to the number of nodes in the CiteSeer dataset. The top row is in accuracy, and the bottom row is the cross-entropy loss.

that there are no training and testing sets, we randomly partitioned the datasets and used 90% of the samples for training and the remaining 10% for testing.

F.2.6 Coauthors Physics dataset

For the Physics dataset, we used the standard one, which can be obtained running `torch_geometric.datasets.Coauthor(root="./data", name='Physics')`. In this case, given that there are no training and testing sets, we randomly partitioned the datasets and used 90% of the samples for training and the remaining 10% for testing.

F.2.7 Heterophilous Amazon ratings dataset

For the Amazon dataset, we used the standard one, which can be obtained running `torch_geometric.datasets.HeterophilousGraphDataset(root="./data", name='Amazon')`. In this case, we used the 10 different splits that the dataset has assigned.

Type	Lay.	Feat.	Slope	Point	Pearson Correlation Coefficient
Accuracy	2	16	$-1.699e-01$	$1.972e+00$	$-9.518e-01$
Accuracy	2	32	$-1.856e-01$	$1.978e+00$	$-9.714e-01$
Accuracy	2	64	$-1.749e-01$	$1.966e+00$	$-9.534e-01$
Accuracy	3	16	$-1.585e-01$	$1.956e+00$	$-9.721e-01$
Accuracy	3	32	$-1.659e-01$	$1.963e+00$	$-9.721e-01$
Accuracy	3	64	$-1.658e-01$	$1.967e+00$	$-9.702e-01$
Loss	2	16	$-1.049e-01$	$7.757e-01$	$-5.924e-01$
Loss	2	32	$-1.762e-01$	$7.646e-01$	$-7.981e-01$
Loss	2	64	$-2.186e-01$	$8.384e-01$	$-9.120e-01$
Loss	3	16	$-1.802e-01$	$1.169e+00$	$-8.345e-01$
Loss	3	32	$-1.629e-01$	$1.200e+00$	$-8.767e-01$
Loss	3	64	$-5.917e-02$	$1.283e+00$	$-2.562e-01$

Table 5: Details of the linear approximation of the CiteSeer Dataset. Note that in this case we used all the values given that the training accuracy is 100% for all nodes.

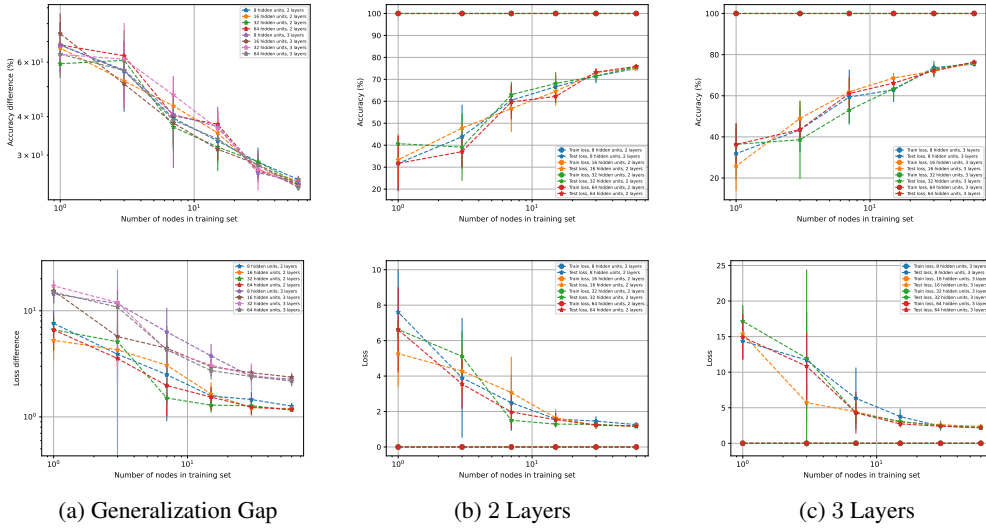


Figure 14: Generalization gap, testing, and training losses with respect to the number of nodes in the PubMed dataset. The top row is in accuracy, and the bottom row is the cross-entropy loss.

F.2.8 Heterophilous Roman Empire dataset

For the Roman dataset, we used the standard one, which can be obtained running `torch_geometric.datasets.HeterophilousGraphDataset(root="./data", name='Roman')`. In this case, we used the 10 different splits that the dataset has assigned.

Type	Lay.	Feat.	Slope	Point	Pearson Correlation Coefficient
Accuracy	2	16	$-2.523e-01$	$1.834e+00$	$-9.942e-01$
Accuracy	2	32	$-2.433e-01$	$1.812e+00$	$-9.583e-01$
Accuracy	2	64	$-2.764e-01$	$1.869e+00$	$-9.761e-01$
Accuracy	3	16	$-2.748e-01$	$1.844e+00$	$-9.910e-01$
Accuracy	3	32	$-2.661e-01$	$1.861e+00$	$-9.712e-01$
Accuracy	3	64	$-2.558e-01$	$1.827e+00$	$-9.890e-01$
Loss	2	16	$-4.166e-01$	$7.695e-01$	$-9.718e-01$
Loss	2	32	$-4.733e-01$	$7.852e-01$	$-9.137e-01$
Loss	2	64	$-4.368e-01$	$7.547e-01$	$-9.718e-01$
Loss	3	16	$-4.424e-01$	$1.067e+00$	$-9.549e-01$
Loss	3	32	$-5.518e-01$	$1.223e+00$	$-9.655e-01$
Loss	3	64	$-5.246e-01$	$1.169e+00$	$-9.632e-01$

Table 6: Details of the linear approximation of the PubMed Dataset. Note that in this case we used all the values given that the training accuracy is 100% for all nodes.

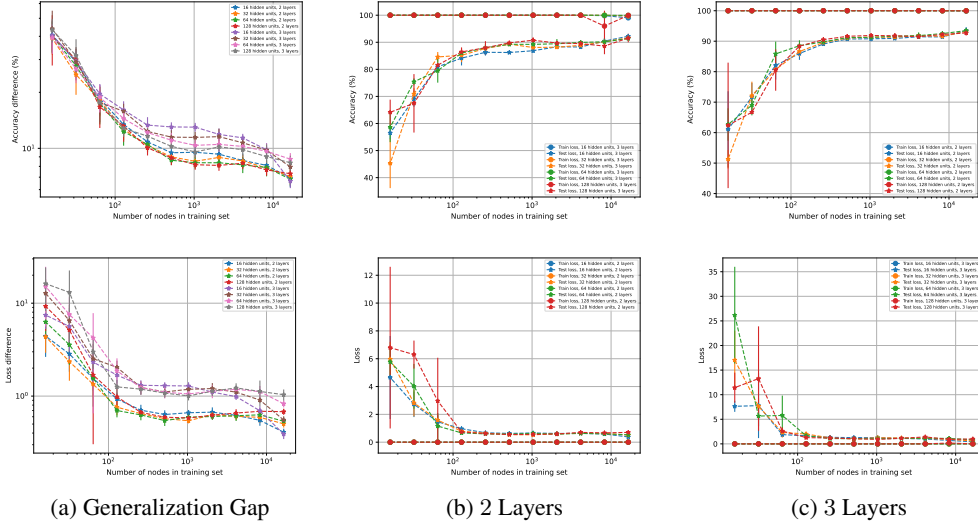


Figure 15: Generalization gap, testing, and training losses with respect to the number of nodes in the CS dataset. The top row is in accuracy, and the bottom row is the cross-entropy loss.

Type	Lay.	Feat.	Slope	Point	Pearson Correlation Coefficient
Accuracy	2	32	$-2.138e-01$	$1.659e+00$	$-9.007e-01$
Accuracy	2	64	$-2.250e-01$	$1.685e+00$	$-8.969e-01$
Accuracy	3	32	$-1.979e-01$	$1.695e+00$	$-9.009e-01$
Accuracy	3	64	$-1.862e-01$	$1.646e+00$	$-8.980e-01$
Loss	2	32	$-2.523e-01$	$6.273e-01$	$-8.244e-01$
Loss	2	64	$-2.933e-01$	$7.762e-01$	$-7.925e-01$
Loss	3	32	$-3.558e-01$	$1.207e+00$	$-8.924e-01$
Loss	3	64	$-3.560e-01$	$1.256e+00$	$-8.568e-01$

Table 7: Details of the linear approximation of the CS Dataset. Note that in this case we used all the values given that the training accuracy is 100% for all nodes.

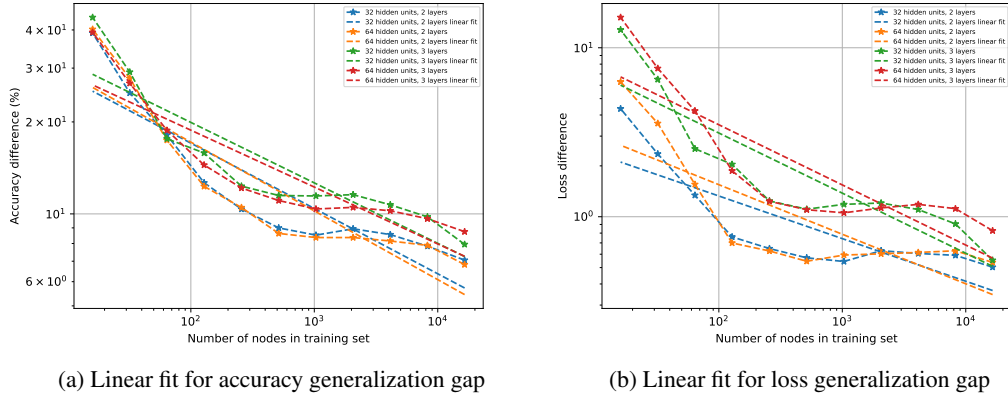


Figure 16: Generalization gaps as a function of the number of nodes in the training set in the CS dataset.

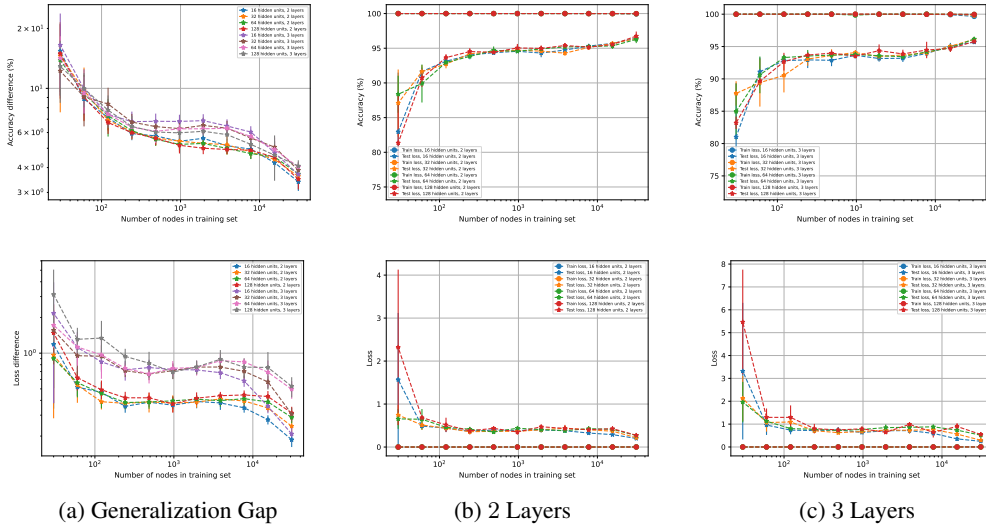


Figure 17: Generalization gap, testing, and training losses with respect to the number of nodes in the Physics dataset. The top row is in accuracy, and the bottom row is the cross-entropy loss.

Type	Lay.	Feat.	Slope	Point	Pearson Correlation Coefficient
Accuracy	2	32	$-1.524e-01$	$1.235e+00$	$-9.064e-01$
Accuracy	2	64	$-1.478e-01$	$1.218e+00$	$-9.145e-01$
Accuracy	3	32	$-1.227e-01$	$1.190e+00$	$-9.328e-01$
Accuracy	3	64	$-1.268e-01$	$1.200e+00$	$-8.826e-01$
Loss	2	32	$-1.111e-01$	$-5.257e-02$	$-7.591e-01$
Loss	2	64	$-9.684e-02$	$-7.335e-02$	$-7.696e-01$
Loss	3	32	$-1.410e-01$	$2.875e-01$	$-8.280e-01$
Loss	3	64	$-1.068e-01$	$2.388e-01$	$-7.679e-01$

Table 8: Details of the linear approximation of the Physics Dataset. Note that in this case we used all the values given that the training accuracy is 100% for all nodes.

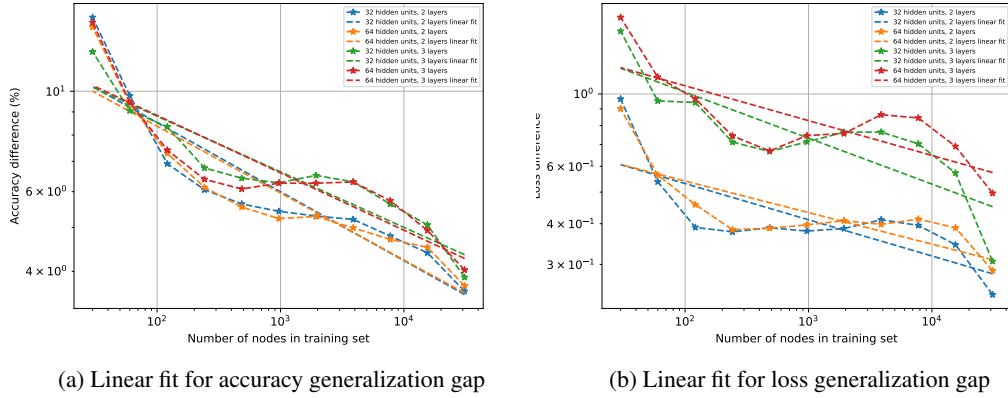


Figure 18: Generalization Gaps as a function of the number of nodes in the training set in the Physics dataset.

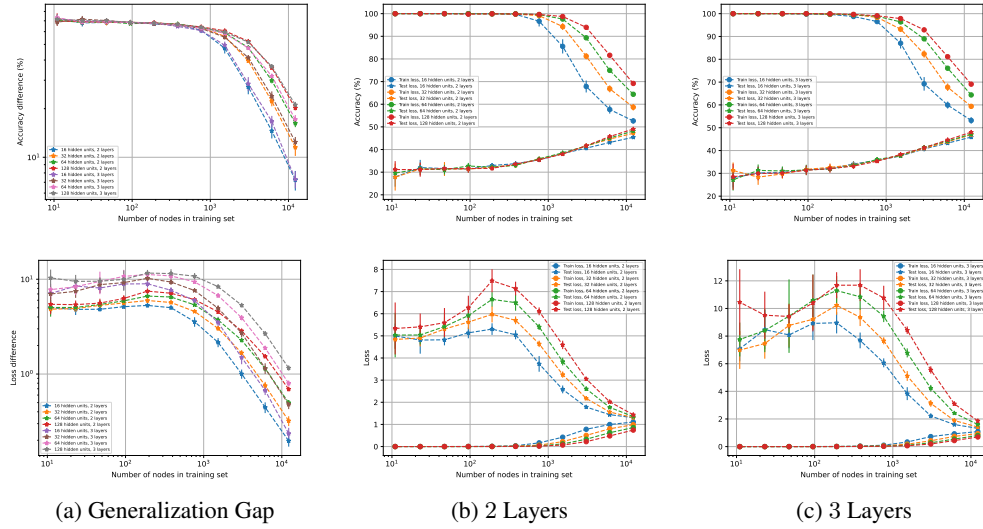


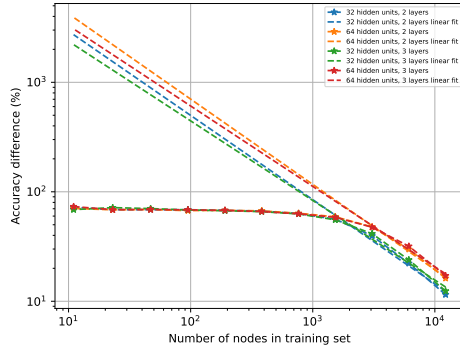
Figure 19: Generalization gap, testing, and training losses with respect to the number of nodes in the Amazon dataset. The top row is in accuracy, and the bottom row is the cross-entropy loss.

Type	Lay.	Feat.	Slope	Point	Pearson Correlation Coefficient
Accuracy	2	32	$-7.693e-01$	$4.236e+00$	$-9.914e-01$
Accuracy	2	64	$-7.788e-01$	$4.404e+00$	$-9.972e-01$
Accuracy	3	32	$-7.268e-01$	$4.101e+00$	$-9.868e-01$
Accuracy	3	64	$-7.354e-01$	$4.257e+00$	$-9.921e-01$
Loss	2	32	$-1.086e+00$	$3.971e+00$	$-9.968e-01$
Loss	2	64	$-1.096e+00$	$4.189e+00$	$-9.985e-01$
Loss	3	32	$-1.134e+00$	$4.339e+00$	$-9.965e-01$
Loss	3	64	$-1.154e+00$	$4.629e+00$	$-9.991e-01$

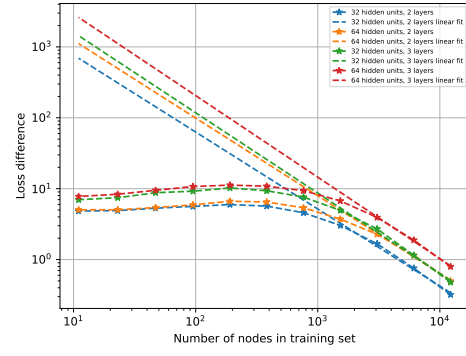
Table 9: Details of the linear approximation of the Amazon Dataset. Note that in this case we used only the values of the generalization gap whose training error is below 95%.

G Further references

Graphon theory Related to the manifold model we consider, some works construct graphs sampled from graphons, which can be seen as a random limit graph model. This line of work has concentrated

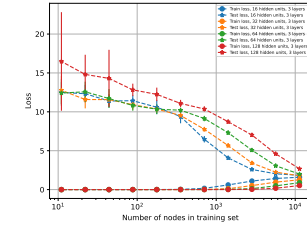
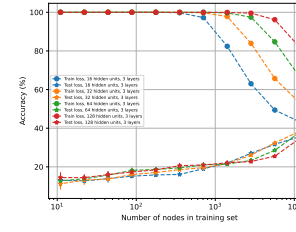
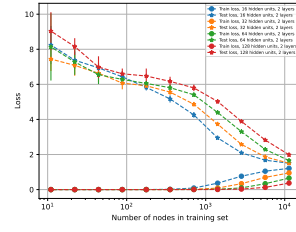
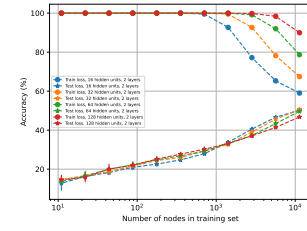
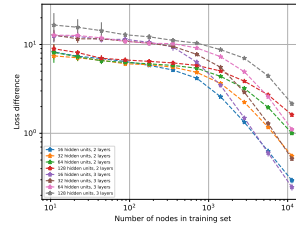
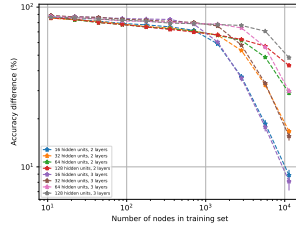


(a) Linear fit for accuracy generalization gap



(b) Linear fit for loss generalization gap

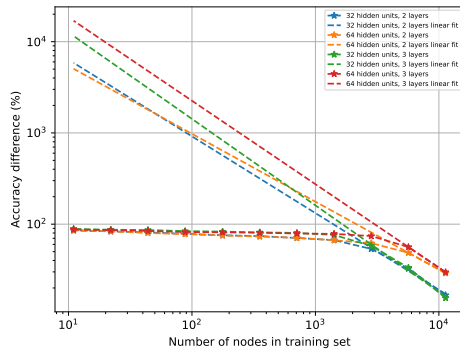
Figure 20: Generalization Gaps as a function of the number of nodes in the training set in the Amazon dataset.



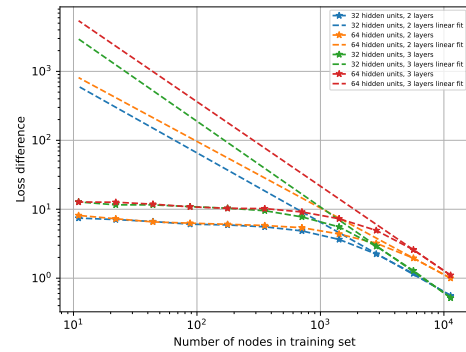
(a) Generalization Gap

(b) 2 Layers

(c) 3 Layers



(a) Linear fit for accuracy generalization gap



(b) Linear fit for loss generalization gap

Figure 22: Generalization Gaps as a function of the number of nodes in the training set in the Roman dataset.

Type	Lay.	Feat.	Slope	Point	Pearson Correlation Coefficient
Accuracy	2	32	$-8.408e-01$	$4.644e+00$	$-9.963e-01$
Accuracy	2	64	$-7.435e-01$	$4.477e+00$	$-1.000e+00$
Accuracy	3	32	$-9.476e-01$	$5.049e+00$	$-9.956e-01$
Accuracy	3	64	$-9.145e-01$	$5.182e+00$	$-1.000e+00$
Loss	2	32	$-1.006e+00$	$3.829e+00$	$-9.992e-01$
Loss	2	64	$-9.656e-01$	$3.915e+00$	$-1.000e+00$
Loss	3	32	$-1.244e+00$	$4.764e+00$	$-9.994e-01$
Loss	3	64	$-1.225e+00$	$5.011e+00$	$-1.000e+00$

Table 10: Details of the linear approximation of the Roman Dataset. Note that in this case we used only the values of the generalization gap whose training error is below 95%

on their convergence, stability and transferability properties [54–56]. Graphon is also used as a tool for pooling in GNNs in [57]. Albeit useful as a model, the graphon presents several limitations compared to the manifold model we use. Firstly, the graphon model assumes an infinite degree at every node [58], which is not the case in the manifold model. Secondly, the graphon presents little intuition on the underlying model, outside of the stochastic block model graphon, it is not trivial to visualize a graphon. On the other hand, manifolds are more interpretable, as can be the case on the sphere, or on other shapes (see Figure 2). Lastly, the manifold model is a more realistic assumption in the types of models that it can characterize.

Transferability of GNNs Transferability of GNNs has been analyzed in many works by comparing the output differences of GNNs on different sizes of graphs when graphs converge to a limit model without statistical generalization analysis. In [15, 54, 55], the transferability of GNNs on graphs generated from graphon models is analyzed with difference bounds of GNN outputs proved. In [59], the authors show how increasing the size of the graph as the GNN learns, generalizes to the large-scale graph. In [60], the authors analyze the transferability of GNNs on graphs generated from a general topological space while the authors in [35] focus on graphs generated from manifolds. In [61], the authors propose a novel graphop operator as a limit model for both dense and sparse graphs with a transferability result proved. In [62] and [63], the authors study the transfer learning of GNNs with measurements of distance between graphs without a limit assumption. In [64], a transferable graph transformer is proposed and proved with empirical results.